# Infrared Colors of the Gamma-ray-detected Blazars

The Astrophysical Journal, 748:68 (14pp), 2012 March 20 doi:10.1088/0004-637X/748/1/68


# INFRARED COLORS OF THE GAMMA-RAY-DETECTED BLAZARS

R. D'Abrusco[1], F. Massaro[2], M. Ajello[2], J. E. Grindlay[1], Howard A. Smith[1], and G. Tosti[2,3,4]
[1] Harvard-Smithsonian Astrophysical Observatory, 60 Garden Street, Cambridge, MA 02138, USA
[2] SLAC National Laboratory and Kavli Institute for Particle Astrophysics and Cosmology, 2575 Sand Hill Road, Menlo Park, CA 94025, USA
[3] Dipartimento di Fisica, Universitadegli Studi di Perugia, 06123 Perugia, Italy
[4] Istituto Nazionale di Fisica Nucleare, Sezione di Perugia, 06123 Perugia, Italy
*Received 2011 September 16; accepted 2012 January 11; published 2012 March 6*

## ABSTRACT

Blazars constitute the most enigmatic class of extragalactic $\gamma$-ray sources, and their observational features have been ascribed to a relativistic jet closely aligned to the line of sight. They are generally divided in two main classes: the BL Lac objects (BL Lacs) and the flat-spectrum radio quasars (FSRQs). In the case of BL Lacs the double-bumped spectral energy distribution (SED) is generally described by the synchrotron self-Compton (SSC) emission, while for the FSRQs it is interpreted as due to external Compton (EC) emission. Recently, we showed that in the [3.4]–[4.6]–[12] $\mu$m color–color diagram the blazar population covers a distinct region (i.e., the *WISE blazar Strip* (WBS)) clearly separated from the other extragalactic sources that are dominated by thermal emission. In this paper, we investigate the relation between the infrared and $\gamma$-ray emission for a subset of confirmed blazars from the literature, associated with *Fermi* sources, for which *WISE* archival observations are available. This sample is a proper subset of the sample of sources used previously, and the availability of *Fermi* data is critical to constrain the models on the emission mechanisms for the blazars. We found that the selected blazars also lie on the WBS covering a narrower region of the infrared color–color planes than the overall blazar population. We then found an evident correlation between the IR and $\gamma$-ray spectral indices expected in the SSC and EC frameworks. Finally, we determined the ratio between their $\gamma$-ray and infrared fluxes, a surrogate of the ratio of powers between the inverse Compton and the synchrotron SED components, and used such parameter to test different blazar emitting scenarios.

*Key words:* BL Lacertae objects: general – gamma rays: galaxies – infrared: galaxies – radiation mechanisms: non-thermal

*Online-only material:* color figures

## 1. INTRODUCTION

Blazars are an intriguing class of active galactic nuclei (AGNs), dominated by non-thermal radiation over the entire electromagnetic spectrum. Their emission extends from radio to TeV energies with a broadband spectral energy distribution (SED) typically described by two main components, the first peaking from IR to X-ray bands while the second often dominating the $\gamma$-ray energy range in which blazars are the most commonly detected extragalactic sources (e.g., Abdo et al. 2010; Massaro et al. 2011b).

The distinguishing observational properties of blazars also include flat radio spectra, high observed luminosity coupled with rapid variability at all frequencies, and highly variable radio to optical polarization. In particular, they are a dominant class of extragalactic sources at radio, microwave, and $\gamma$-ray frequencies where thermal emission processes do not produce significant amounts of radiation (Giommi et al. 2011). Adopting the blazar classification scheme given in the ROMA-BZCAT catalog[5] (Massaro et al. 2009, 2010), based on the width of optical spectral lines, blazars usually come in two flavors: the BL Lac objects (BL Lacs) and flat-spectrum radio quasars (FSRQs), with the latter more or less equivalent to the former population except for stronger emission lines, higher radio to optical polarization, and higher redshift. In addition, the high-energy component of blazar SED is usually found in the GeV band for FSRQs, while it can extend to TeV energy for BL Lacs. Hereafter, we adopt the naming convention of the ROMA-BZCAT catalog, referring to BL Lacs as BZBs and to the FSRQs as BZQs.

These extreme features have been interpreted as radiation arising from a relativistic jet closely aligned to the line of sight and emitting continuous, Doppler-boosted spectra (Blandford & Rees 1978). For both classes of blazars, according to the widely accepted synchrotron self-Compton (SSC) scenario, the low-energy component is produced by inverse synchrotron emission from highly relativistic electrons, while the high-energy bump can be attributed to inverse Compton scattering of synchrotron photons by the same population of relativistic electrons that produce the synchrotron emission (Marscher & Gear 1985; Inoue & Takahara 1996). A different theoretical interpretation of the high-energy $\gamma$-ray bump characteristic of the BZQ broadband emission invokes the inverse Compton emission of seed photons arising from regions external to the jet (e.g., the broad-line region, accretion disk) as emission mechanism for such feature of the SED. This model is known as the external Compton scenario (EC; e.g., Dermer & Schlickeiser 2002; Cavaliere & D'Elia 2002).

Recently, we showed that in the [3.4]−[4.6]−[12] $\mu$m color–color diagram the blazars, which are dominated by non-thermal emission mechanism, cover a distinct region (hereafter the *WISE blazar Strip* (WBS)), well separated from the locus of other extragalactic sources which are dominated by the contribution of thermal radiation (Massaro et al. 2011a).

This result has been obtained using the blazars listed in the ROMA-BZCAT catalog. In the IR, we used data from *WISE* (Wright et al. 2010). The *WISE* mission observed the sky at 3.4, 4.6, 12, and 22 $\mu$m in 2010 with an angular resolution of $6''.1$, $6''.4$, $6''.5$, and $12''.0$ in the four bands, achieving 5$\sigma$ point source sensitivities of 0.08, 0.11, 1, and 6 mJy in unconfused regions on the ecliptic, respectively (Wright et al. 2010). The

[5] http://www.asdc.asi.it/bzcat/

astrometric accuracy of *WISE* is ∼0″.50, 0″.26, 0″.26, and 1″.4 for the four *WISE* bands, respectively (Cutri et al. 2011).

A previous attempt to compare the infrared behavior of blazars with normal galaxies in the $J - H - K$ color–color diagram was performed using the Two Micron All Sky Survey (2MASS) archival data (e.g., Chen et al. 2005). However, our new approach has three advantages over the study performed using 2MASS: (1) mid-IR selection is dominated by dusty objects, in particular spiral and starburst galaxies; (2) the blazar population covers a noticeably narrow region in the [3.4]–[4.6]–[12] $\mu$m color–color plot that is clearly statistically separated from the locus dominated by other extragalactic sources (Massaro et al. 2011a); and (3) *WISE* covers a much larger interval of frequencies and reaches to larger wavelengths than 2MASS, yielding a color–color distribution where stars occupy a narrow and well-defined locus.

The *Fermi* Large Area Telescope (LAT) Collaboration has recently released the *Fermi*-LAT second source catalog (2FGL; e.g., The *Fermi*-LAT Collaboration 2011) including about 800 $\gamma$-ray sources associated with blazars to a high level of confidence; 571 of these blazars are also present in the ROMA-BZCAT. In this paper, we investigate how the infrared emission of blazars is related to their high-energy $\gamma$-ray radiation by cross-matching the sample of ROMA-BZCAT blazars associated with *Fermi* sources with the *WISE* data archive (Wright et al. 2010). In Section 2, we present the blazar sample used throughout our investigation. In Section 3, we show how the *Fermi*-detected blazars lie on the WBS and we determine the distributions of their IR colors. Then, in Section 4, we investigate a possible relation between the blazar IR and $\gamma$-ray emissions, as predicted in the SSC and EC radiative scenarios. In Section 5, we estimate the Compton dominance (CD) parameter for both the BZQs and the BZBs and we also examine the apparent correlation between the CD and the $\gamma$-ray spectral index for BZBs. In Section 6, we focus our analysis on the BL Lac population and its subclasses. Finally, our summary and discussion are given in Section 7.

Throughout this paper, we assume that the spectral indices, $\alpha$, are defined by flux density, $S_\nu \propto \nu^{-\alpha}$. Unless otherwise stated, we use cgs units.

## 2. SAMPLE SELECTION

We considered all the blazars in the ROMA-BZCAT that have been associated with a *Fermi* source, as reported in the 2FGL (The *Fermi*-LAT Collaboration 2011), for a total number of 571 sources (i.e., 330 BZBs and 241 BZQs). The second edition of the ROMA-BZCAT catalog (Massaro et al. 2009) assembles blazars known in the literature and carefully verified by inspection of their multi-wavelength emission. Members of the ROMA-BZCAT catalog are selected on the basis of a set of criteria involving the presence of detection in the radio band down to 1 mJy flux density at 1.4 GHz (2.1 $\mu$m), the optical identification and availability of an optical spectrum for further spectral classification, and the detection of X-ray luminosity $L_X \geqslant 10^{43}$ erg s$^{-1}$. Such criteria do not produce a statistically homogeneous or complete sample of blazars because of the spatially uneven distribution and the variable depths of observations available, but provides the largest and most carefully selected sample of confirmed blazars available to date. The selection and spectral classification of blazars can be difficult due to the absence of typical spectral emission features and to the variability of the emission on timescales of a day or even a few hours. In the ROMA-BZCAT, blazars are also classified into three classes, based on the prominence of the emission features in the optical spectra of these sources. The three classes of such classification are: BZB for the BL Lac sources, i.e., AGNs with featureless optical spectra and narrow emission lines; BZQ for FSRQs with optical spectra showing broad emission lines and typical blazar behavior; BZU for blazars of uncertain type, associated with sources with peculiar characteristics but also showing typical traits of the blazars. This spectral classification will be used throughout this paper. The distinction between BZB and BZQ depends on the choice of an arbitrary threshold value of the equivalent width of the emission lines in the optical spectra of the sources.

The 2FLG catalog contains primarily unresolved sources detected in the all-sky *Fermi* observations obtained throughout the second year of operation. The sources, after detection and the localization in the sky, are assigned an integrated flux in the 100 MeV–100 GeV energy range, a spectral shape, and a significance parameter *TS* based on how significantly each source emerges from the background. Only sources with $TS \geqslant 25$, corresponding to a significance of $4\sigma$, have been included in the catalog. Each of the 1873 2FLG sources has been considered for identification with already known astronomical sources available in the literature on multi-wavelength observations (The *Fermi*-LAT Collaboration 2011). For 127 of the 2FLG sources firm identifications have been produced (namely, reliable identifications based on synchronous periodic variability of the sources, coincident spatial morphologies for extended sources, or correlated aperiodic variability). The remaining sources have been investigated for association with sources contained in a list of source catalogs based on different multi-wavelength observations. The ROMA-BZCAT catalog is one of the catalogs used for the association of the 2FLG sources, and 571 *Fermi* sources have been associated with a BZCAT-ROMA blazar.

We selected all blazars in the ROMA-BZCAT reliably associated with a $\gamma$-ray source of the 2FGL catalog. Then, using the more accurate radio position of the ROMA-BZCAT in place of the coordinates from the *Fermi* catalog, we searched for infrared counterparts of the above blazars in the *WISE* archive.

The total number of ROMA-BZCAT blazars in the 2FGL footprint falling in the area surveyed by *WISE* during the first year (corresponding to 57% of the whole sky) is 332 (mostly due to the incompleteness of the sky coverage of the ROMA-BZCAT). In order to search for the positional coincidences of blazars in the observed *WISE* sky, we considered a search radius 2″.4, obtained by combining the 1″ error assumed for the radio position reported in the ROMA-BZCAT (Massaro et al. 2009) with the error on the fourth *WISE* band at 22 $\mu$m (i.e., 1″.4; see also Wright et al. 2010 for more details). Using a conservative approach in our analysis, we only considered sources in the *WISE* Preliminary Source Catalog (WPSC)[6] with a minimum signal-to-noise ratio (S/N) of 7 in at least one of the four infrared bands.

The number of *Fermi*-BZCAT blazars with a *WISE* counterpart within the first region of 2″.4 is 296, corresponding to ∼45% of the *Fermi*–*WISE* blazar sample in the WPSC, detected with a chance probability of ∼3% (see Maselli et al. 2011; Massaro et al. 2011a for more details) We did not find any multiple matches using 2″.4 as search radius. We have used only these 296 blazars for our investigation. The remaining 12 sources with no apparent corresponding *WISE* sources within 2″.4 can be associated with at least one source contained in the *WISE* catalog using a search radius of 12″, but have not been

[6] http://wise2.ipac.caltech.edu/docs/release/prelim/preview.html

used in our study. By definition, the *Fermi–WISE* blazar sample is a proper subset of the sample of ROMA-BZCat blazars with *WISE* counterparts discussed in the previous paper (Massaro et al. 2011a). The table containing the main parameters of the 296 sources of the *Fermi–WISE* blazar sample is can be found in Appendix B.

## 3. THE *FERMI* BLAZARS AT INFRARED FREQUENCIES

As recently shown in Massaro et al. (2011a), the blazars, dominated in the infrared by their synchrotron emission, lie in a distinct region of the [3.4]−[4.6]−[12] $\mu$m color–color diagram, and appear to be distinctly separated from the rest of the non-synchrotron-dominated sources populating the sky as observed by *WISE*. We randomly selected 14 not-overlapping regions of 4 deg$^2$ each for a total 56 deg$^2$ at high Galactic latitude (Massaro et al. 2011a), within the 116 deg$^2$ considered in the WPSC (Cutri et al. 2011). We collected all of the 453,420 sources detected by *WISE* in its first year catalog (hereafter called *WISE* thermal sources because most of them are dominated by thermal emission in the infrared energy range), having an S/N $>$ 7 in at least one band, a conservative level for the WPSC release to emphasize the catalog reliability[3] (Cutri et al. 2011). We have not excluded the stars from the sample of generic *WISE*-detected sources in the color–color diagrams shown in this paper, since at high galactic latitude, the majority of the observed sources are extragalactic with only little contamination from stars, and we have checked that their presence does not negatively affect the conclusions about the separation of the region of color space occupied by *Fermi*-detected blazars.

We built the [3.4]–[4.6]–[12] $\mu$m color–color diagrams from the magnitudes reported in the *WISE* catalog[7] for all the *WISE* thermal sources in the 56 deg$^2$ area described above, and for all the sources in the *Fermi–WISE* blazar sample. In Figure 1, we also show the location of different classes of objects and overlaid to five levels' isodensity contours for all the *WISE* thermal sources in the 56 deg$^2$ region. We plot the blazars of the diagram to characterize their infrared emission. Figure 1 shows that the *Fermi–WISE* blazars lie in an even more confined region than the general WBS shown in Figure 1 of Massaro et al. (2011a). We note that the relative errors for both the infrared colors are less than 10% for 97% of the *Fermi–WISE* blazar sample but less than 5% for ∼85% of the sources.

The subregion of the WBS occupied by the *Fermi–WISE* blazars is well defined. Only two "outliers" out of a total number of 296 blazars are visible in this color–color plane: 2FGL J1506.6+0806 and 2FGL J1550.7+0526 (also known as 4C +05.64 or PKS 1548+056). While for these two specific sources the possibility of a wrong association in the 2FGL catalog cannot be ruled out, in general a possible explanation for these or other ROMA-BZCAT sources to lie outside of the WBS might be a thermal contribution from their host galaxy that is non-negligible with respect to the non-thermal IR emission. In general, however, the blazars of the *Fermi–WISE* blazar sample, dominated by synchrotron emission in the IR, are located in distinctly defined regions of the *WISE* color–color planes all well separated from the other non-synchrotron-dominated sources detected by *WISE*.

Assuming that the infrared spectrum of the sources in the *Fermi–WISE* blazar sample can be described by a power law, we derive the relation between the infrared colors and the spectral

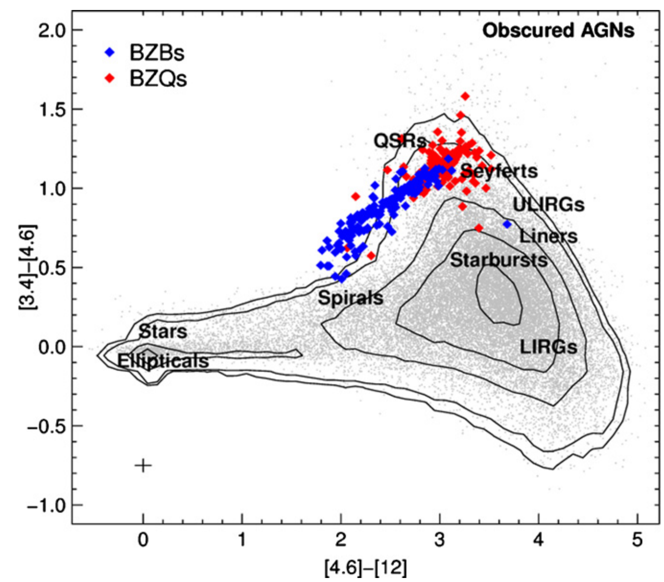


**Figure 1.** [3.4]–[4.6]–[12] $\mu$m color–color diagram of *Fermi–WISE* blazar sample sources. We plot the 296 blazars associated with a *WISE* source within a region of radius 2″.4. The two blazar classes of BZBs (blue) and BZQs (red) are shown. The background gray dots correspond to 453,420 *WISE* sources detected in a region of 56 deg$^2$ at high Galactic latitude. The isodensity curves for the *WISE* sources, corresponding to 50, 100, 500, and 2000 sources per unit area in the color–color plane, respectively, are shown (see Section 3). The location of different classes of objects, namely the quasars (QSRs), the ultraluminous infrared galaxies (ULIRGs), and luminous infrared galaxies (LIRGs) is also shown in the plot.

(A color version of this figure is available in the online journal.)

slope $\alpha$. Considering a source of apparent magnitudes $m_1$, $m_2$, $m_3$, $m_4$ in the four different *WISE* bands, with the zero-point magnitudes $m_{01}$, $m_{02}$, $m_{03}$, and $m_{04}$, respectively, the relation between one color, for example $c_{12} = m_1 - m_2 = [3.4]–[4.6]$, and the associated spectral slope $\alpha_{12}$ can be written as

$$c_{12} = m_1 - m_2 = 2.5\,\alpha_{12}\,\log\left(\frac{\nu_1}{\nu_2}\right) + (m_{01} - m_{02}), \qquad (1)$$

where $\nu_1$ and $\nu_2$ are the frequencies corresponding to the 3.4 and 4.6 $\mu$m wavelengths, respectively. We estimated the values of the spectral indices $\alpha_{12}$, $\alpha_{23}$, and $\alpha_{34}$ from the three infrared colors $c_{12}$, $c_{23}$, and $c_{34}$, respectively. Then we compared their distributions to test for the presence of spectral curvature for the sources in the *Fermi–WISE* blazar sample. We found that the median (1.07, 0.94, and 1.12 for $\alpha_{12}$, $\alpha_{23}$, and $\alpha_{34}$), the peak values (1.06, 0.99, and 1.12), and variances (0.33, 0.22, and 0.26) of the distributions of the three IR spectral indices are consistent with each other. In the following analysis, we will consider the infrared spectral index $\alpha_{IR} = \alpha_{12}$, because the *WISE* 3.4 and 4.6 $\mu$m filters are the most sensitive. Unfortunately, given the *WISE*-restricted energy range we did not find any hint of a curved spectral shape. In Figure 2, we show the distribution of the spectral indices in each band, $\alpha_{12}$, $\alpha_{23}$, and $\alpha_{34}$.

Since the sources in the *Fermi–WISE* blazar sample have been detected in all the four *WISE* infrared bands, we can also construct the [3.4]−[4.6]−[12]−[22] $\mu$m color–color diagram, where the two colors are independent (see Figure 3). In this color–color diagram, the separation between the blazars and the generic *WISE* sources is even more evident than in the [4.6]−[12]−[22] $\mu$m color–color diagram, even though the locus is less narrow than in the case of the [3.4]−[4.6]−[12]−[22] color–color diagram shown in Figure 1). In this plot, we also report the line corresponding to a power-law spectrum of varying

[7] All *WISE* magnitudes are in Vega system.

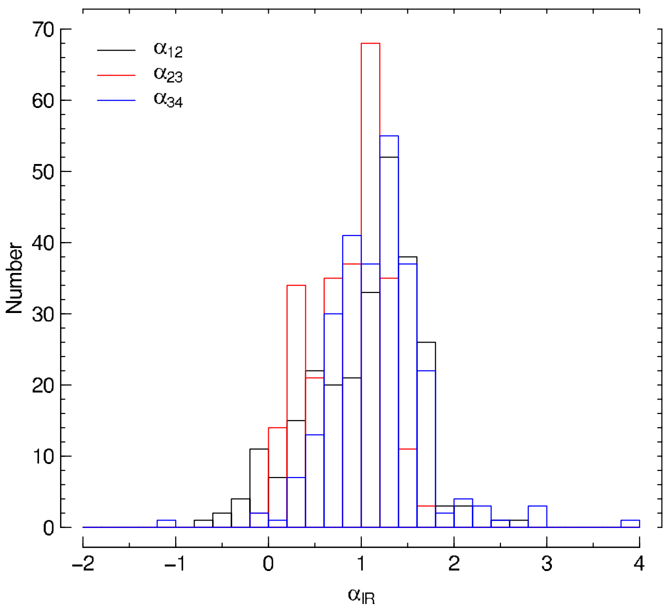


**Figure 2.** Histograms of the distributions of the infrared spectral indices $\alpha_{12}$, $\alpha_{23}$, and $\alpha_{34}$ for the *Fermi–WISE* blazar sample, derived by using Equation (1) for the three different colors (see Section 3 for more details).

(A color version of this figure is available in the online journal.)

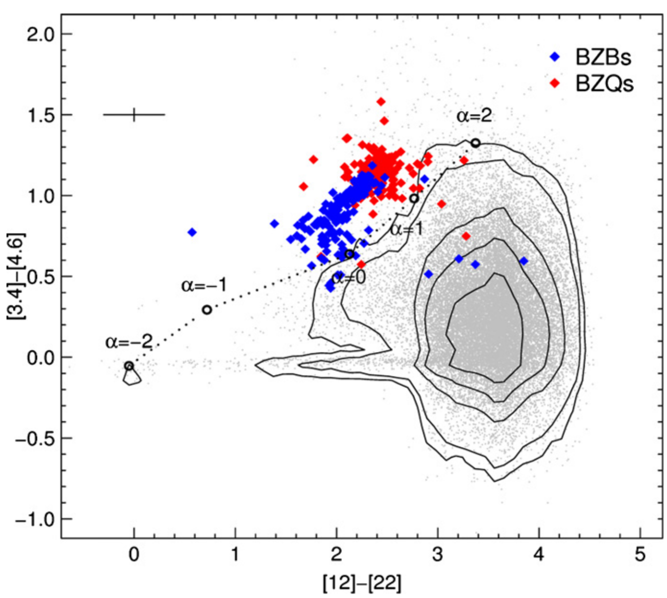


**Figure 3.** Same as Figure 1 but with a different choice of infrared colors: [3.4]−[4.6]−[12]−[22] $\mu$m. We also report the black dashed line corresponding to the IR colors generated by a power-law spectrum of spectral index $\alpha_{\mathrm{IR}}$. The black cross shown in the right bottom represents the typical error bars on the infrared colors (see Section 3 for more details).

(A color version of this figure is available in the online journal.)

indices $\alpha_{\mathrm{IR}}$ described by the equation

$$c_{12} = \left[\frac{\log(\nu_1/\nu_2)}{\log(\nu_3/\nu_4)}(c_{34} - m_{03} + m_{04})\right] + (m_{01} - m_{02}), \qquad (2)$$

where $c_{34} = m_3 - m_4 =$ [12]–[22] is the infrared color corresponding to the bands at 12 $\mu$m and 22 $\mu$m, respectively (see Figure 3).

The remaining [4.6]−[12]−[22] $\mu$m color–color diagram is shown in Appendix A. In particular, we note that in Figure 3 (and Figure 12 in Appendix A), the regions covered by the *Fermi–WISE* blazar sample sources are also clearly separated from the thermal *WISE* sources.

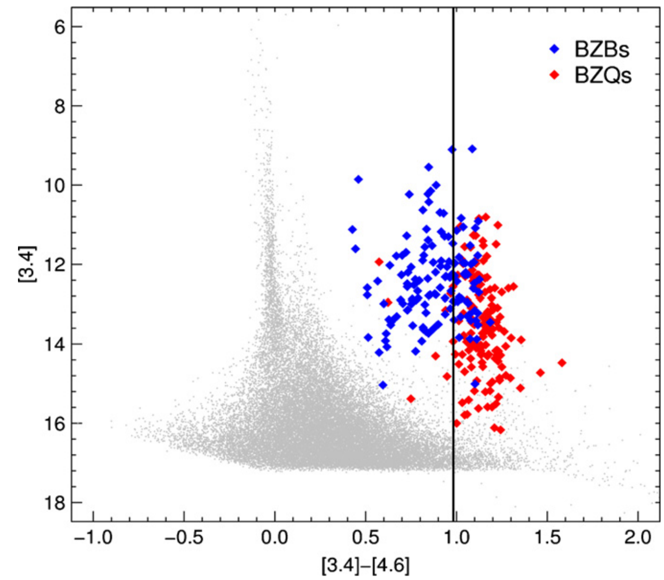


**Figure 4.** Color–magnitude diagram built with the most sensitive infrared *WISE* bands, namely the [3.4]−[4.6] color and the [3.4] magnitude. The BZQ sources clearly show the value of the color [3.4]−[4.6] ∼ 1 corresponding to a spectral index $\alpha_{\mathrm{IR}}$ of −1, as a consequence of the *WISE* observations sampling the peak of their synchrotron components. The black vertical line corresponds to the color value associated with a power law with spectral index $\alpha_\nu = -1$.

(A color version of this figure is available in the online journal.)

Finally, we present a color–magnitude diagram for the three *WISE* bands with highest sensitivity (Figure 4) where the flux limit of the *WISE* survey is clearly visible. In this plot, all *Fermi–WISE* blazar sample sources lie well above the value of the limiting magnitude at 3.4 $\mu$m, and the blazars appear significantly brighter than all the other sources with similar values of the color. Nonetheless, as already discussed for [3.4]−[4.6]−[12]−[22] color–color diagram shown in Figure 1, if on one hand the sources of the *Fermi–WISE* blazar sample are well separated from the *WISE* sources even in this color–magnitude plot, on the other hand the region of the plane occupied by the blazars is less compact and well defined than the WBS visible in the [4.6]−[12] $\mu$m versus [3.4]−[4.6] $\mu$m color–color plane (Figure 1). Other color–magnitude plots of the *Fermi–WISE* blazar sample are shown in Appendix A.

It is worth stressing that ∼95% of the BZQs have [3.4]–[4.6] color larger than the value of the color associated with a power-law spectrum of spectral index 1. This fact suggests that the peaks of the first component (i.e., the synchrotron emission) of these sources occur inside or very close to the *WISE* spectral range. The situation appears to be different for the BZB class, which displays infrared colors ranging between 0.5 and 1.2 (see Section 6 for more details). It is also interesting to note that all the sources in the *Fermi–WISE* blazar sample are consistently above the sensitivity limit of the *WISE* survey, even though this effect is most likely due to the luminosity distribution and selection limits of the *Fermi* observations.

## 4. THE $\alpha_{\mathrm{IR}}$–$\alpha_\gamma$ CORRELATION

According to the SSC or the EC scenarios, usually adopted to interpret the blazar emission, the particles (i.e., electrons) that are emitting via synchrotron radiation at radio and infrared frequencies are also those that are scattering the photons to high energy, in the X-rays and in the $\gamma$-rays, via inverse Compton emission. Consequently, an empirical correlation between the spectral indices and the fluxes in the infrared and in the $\gamma$-ray

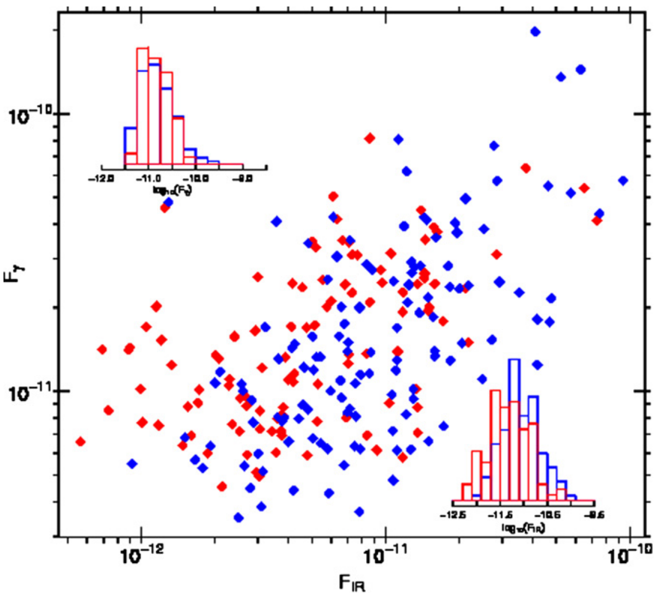


**Figure 5.** Distribution of the sample of 2FGL detected blazars from the BZCAT-ROMA catalog with *WISE* counterparts relative to the total $\gamma$-ray flux (from the 2FGL catalog) and the total IR *WISE* flux calculated from the magnitudes in the four *WISE* filters. BZBs and BZQs according to the spectral classification available in the ROMA-BZCAT catalog are plotted with red and blue, respectively. The histograms of the IR and $\gamma$-day fluxes distributions for the sample of blazars considered are shown in the two insets of the plot. All fluxes are expressed in cgs units.

(A color version of this figure is available in the online journal.)

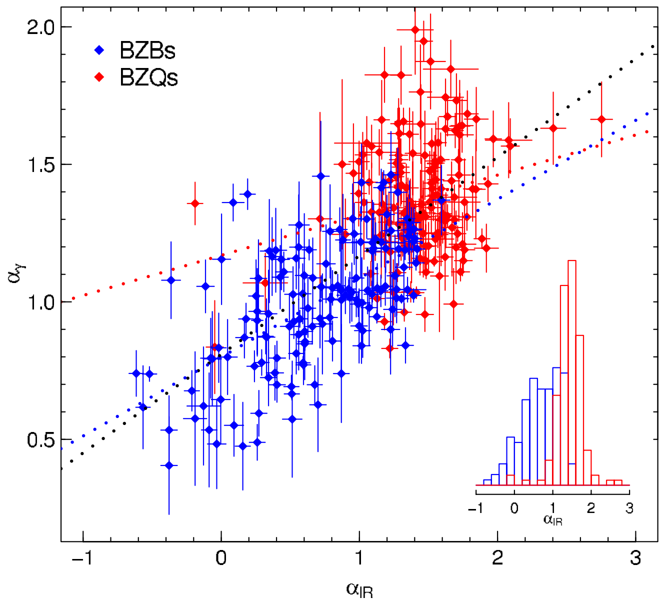


**Figure 6.** Scatterplot of the $\alpha_{\rm IR}$–$\alpha_\gamma$ distribution, with the two classes of blazars BZBs (blue) and BZQs (red) shown. In the inset, the histogram of the two distributions of $\alpha_{\rm IR}$ is plotted, clearly showing the dichotomy between the two classes (see Section 4 for more details). Three linear regression lines with different colors are shown: the black has been obtained by linear fitting on the whole sample of BZBs and BZQs, while the blue and red lines are associated with the regression evaluated for BZBs and BZQs alone, respectively.

(A color version of this figure is available in the online journal.)

energy range is expected, since they originate from the same electron distribution.

The relationships between radio, microwave, and $\gamma$-ray emissions of blazars are discussed by many authors (e.g., Giommi et al. 2011). A positive correlation between the radio and $\gamma$-ray fluxes has been observed, though with large scatter, using several samples (e.g., Kovalev et al. 2009; Giroletti et al. 2010; León-Tavares et al. 2011). However, a correlation between $\gamma$-ray and IR in the spectral range covered by *WISE* had not been observed to date. This could be mainly due to the lack of $\gamma$-ray observations for a sufficiently large number of blazars, now resolved by the availability of *Fermi* data. At the same time, the infrared frequencies observed by *WISE* had not been extensively investigated for blazars despite the fact that the SED frequency peak lies very close to or inside this spectral range, at least for most of the BZQs.

In Figure 5, we show the distribution of the sample of blazars considered in this paper in the plane of the total *Fermi* energy flux in the 100 MeV–100 GeV energy interval obtained by spectral fitting in the same range (from the 2FGL catalog), and of the total *WISE* IR flux derived from the *WISE* magnitudes. The total IR fluxes have been calculated by summing the fluxes in the four *WISE* filter obtained as $\nu f(\nu)$ and accounting for color corrections as discussed in Wright et al. (2010). BZBs and BZQs are plotted with different colors in this plot. A correlation between $\gamma$-ray and IR fluxes is statistically significant for the whole sample of sources (with correlation coefficient $r_s = 0.57$) and for both classes of BZBs and BZQs separately ($r_s = 0.64$ and $r_s = 0.61$, respectively).

In Figure 6, we report the $\alpha_{\rm IR}$–$\alpha_\gamma$ scatterplot with the black line obtained by linear regression on the two spectral indices for BZBs and BZQs together. The associated correlation coefficient is $r_s = 0.71$, corresponding to a negligible; this implies that the two spectral indices are correlated at a very high level of significance. We have also evaluated the best-fitting linear relations for BZBs and BZQs separately (blue and red lines respectively) and the Spearman's correlation coefficients for these two subsamples of sources. While the correlation between the two spectral indices for the BZBs has a high level of significance with $r_s = 0.59$ and negligible $p$-value, the correlation for the BZQs is associated with lower values of the correlation coefficient $r_s = 0.14$, so that the hypothesis that the two parameters are uncorrelated can be rejected at an 80% level of significance. Overall, the correlation between the IR and $\gamma$-ray spectral indices is dominated by the BZBs. The dichotomy between the BZB and BZQ classes of objects is evident from this plot, not only in the $\alpha_\gamma$ distribution and in the comparison of the linear regression lines for the two classes of sources separated (e.g., The *Fermi*-LAT Collaboration 2011), but also in the $\alpha_{\rm IR}$ distribution (see the histogram in Figure 6). We performed a Kolmogorov–Smirnov (K-S) test and we found that the distributions of the $\alpha_{\rm IR}$ for the BZBs and the BZQs differ at 97% level of significance. We also report in Figure 7 the three-dimensional plot of the two main infrared colors used to build the [3.4]−[4.6]−[12] $\mu$m color–color diagram and the $\gamma$-ray spectral index $\alpha_\gamma$, to highlight the distinction between the two classes of blazars. The two colors can be here considered as surrogates of the infrared spectral index $\alpha_{\rm IR}$ (see Section 3 for more details).

## 5. THE COMPTON DOMINANCE

The CD parameter, defined as the ratio between the inverse Compton and synchrotron peak luminosities, can be used to identify the main radiative loss process for the emitting particles, either synchrotron or inverse Compton emission. In particular, since for the majority of the BZQs the *WISE* and the *Fermi* spectral ranges are directly sampling or are very close to the peak frequency for both the inverse Compton and

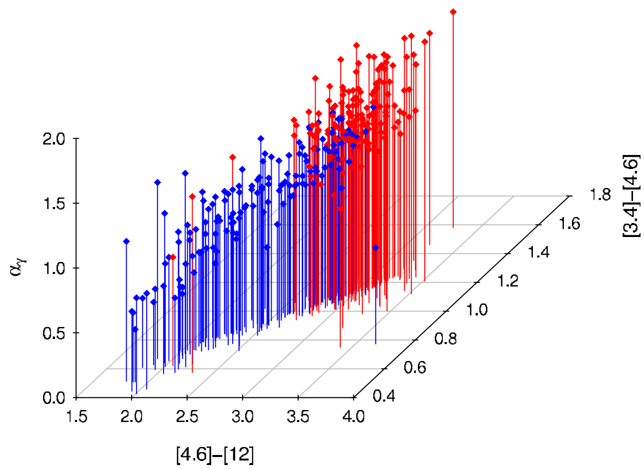


**Figure 7.** Three-dimensional scatterplot of the distribution of *Fermi* blazars in the [4.6]−[12]–[3.4]−[4.6]–$\alpha_\gamma$ space. The two different classes of blazars, namely the BZBs (blue points) and BZQs (red points), are shown (see Section 4 for more details). The lines extending downward are meant to show the position of the projections of the points on the [3.4]−[46] vs. [4.6]−[12] color–color plane.

(A color version of this figure is available in the online journal.)

the synchrotron components, the ratio between the infrared and the $\gamma$-ray fluxes provides a good estimate of the CD parameter for the *Fermi–WISE* blazars' sample sources.

In Figure 8, we show the two distributions of the CD parameter for the different classes of BZBs and BZQs. We performed a K-S test on the CD distributions of BZBs and BZQs and we found that these differ by a 78% level of significance. Finally, we report the relation between the CD parameter and the $\alpha_\gamma$, for both classes of blazars in Figure 9.

## 6. THE TWO FAMILIES OF BL LAC OBJECTS

BL Lacs were originally subclassified into two families on the basis of their radio to X-ray spectral index (Padovani & Giommi 1995). This classification scheme has been recently extended to all types of non-thermal-dominated AGNs (Abdo et al. 2010), on the basis of the position of the peak of the first SED component, generally assumed to be synchrotron emission. This gives rise to the distinction between the *"Low"–"Intermediate"–"High" Synchrotron peaked* non-thermal sources (LSPs, ISPs, HSPs), whenever the peak of the synchrotron component lies below $10^{14}$ Hz ($\sim$3 $\mu$m), between $10^{14}$ Hz and $10^{15}$ Hz ($\sim$0.3 $\mu$m), or higher than $10^{15}$ Hz, respectively (Abdo et al. 2010). Even if blazars should most appropriately be classified on the basis of a complete SED, built with simultaneous data, this is not possible in the majority of the cases, but LSP or HSP BL Lacs can still be identified by using radio–optical–X-ray spectral indices (Padovani et al. 2003; Giommi et al. 2005). The frequency of the synchrotron peak is estimated using the broadband spectral indices between radio and optical wavelengths ($\alpha_{ro}$) and the optical and X-ray wavelengths ($\alpha_{ox}$) and extrapolating the spectral shape of BL Lacs to infrared frequency, where the peak is expected to be located according to accepted BL Lacs SED

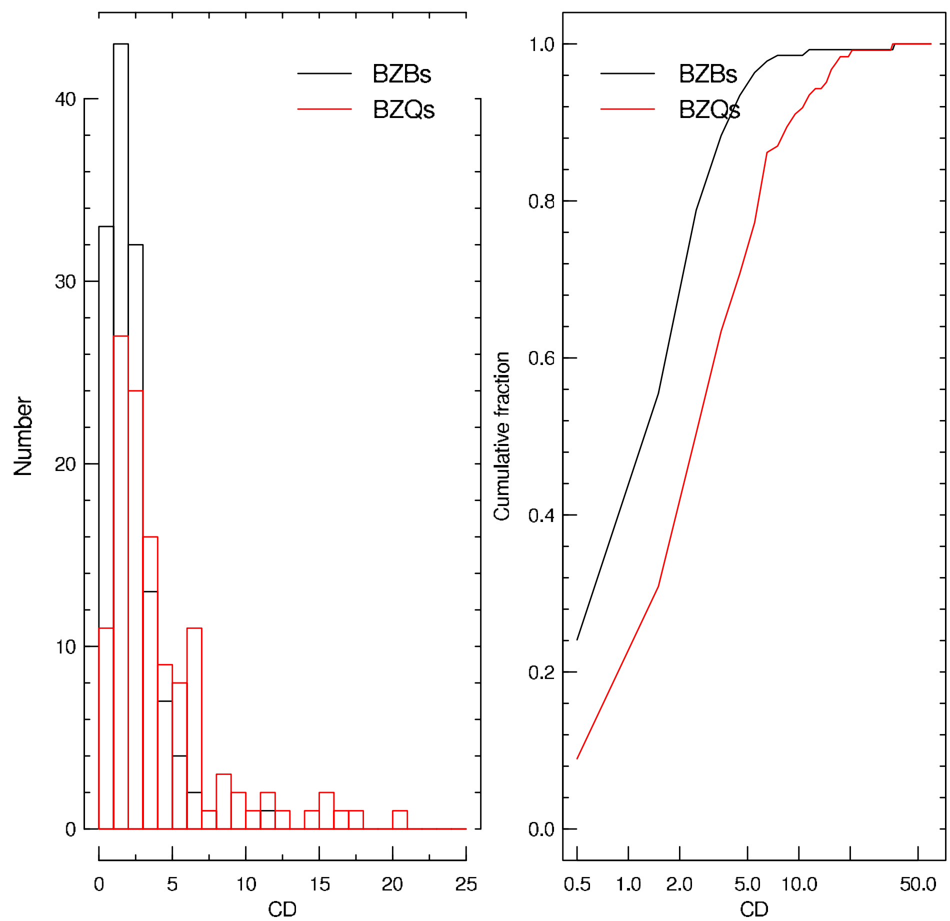


**Figure 8.** Histogram of the distributions of the CD parameter for the BZBs (black) and the BZQs (blue) (left panel), and their cumulative distribution (right panel; see Section 5 for more details).

(A color version of this figure is available in the online journal.)

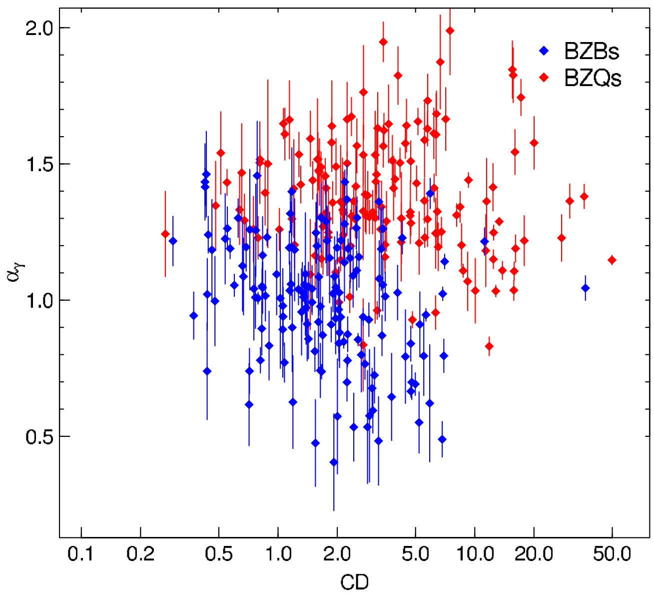


**Figure 9.** Scatterplot of the $\alpha_\gamma$ and the CD parameter for the BZBs (blue symbols) and the BZQs (red symbols).

(A color version of this figure is available in the online journal.)

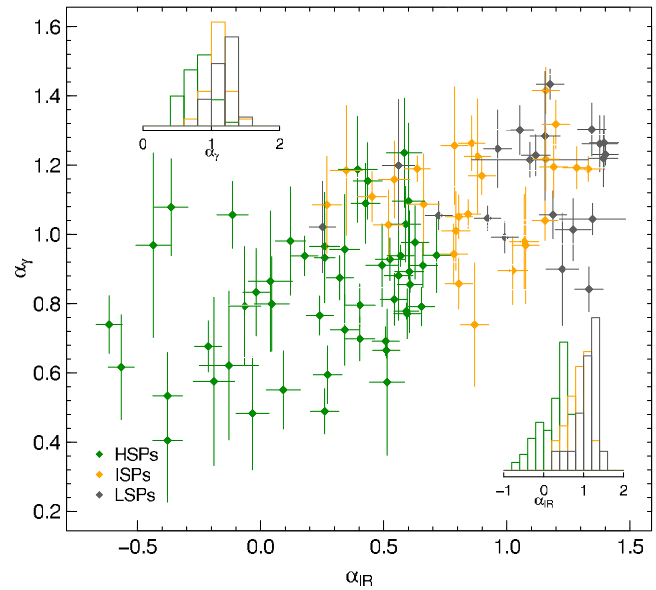


**Figure 10.** Scatterplot of the $\alpha_{IR}$–$\alpha_\gamma$ distribution for BL Lacs. The three BL Lac subclasses of HSPs (green points), LSPs (black points), and ISPs (yellow points) are shown. We also report the histogram of the two distributions of $\alpha_{IR}$ and $\alpha_\gamma$ that clearly show the dichotomy between the three subclasses.

(A color version of this figure is available in the online journal.)

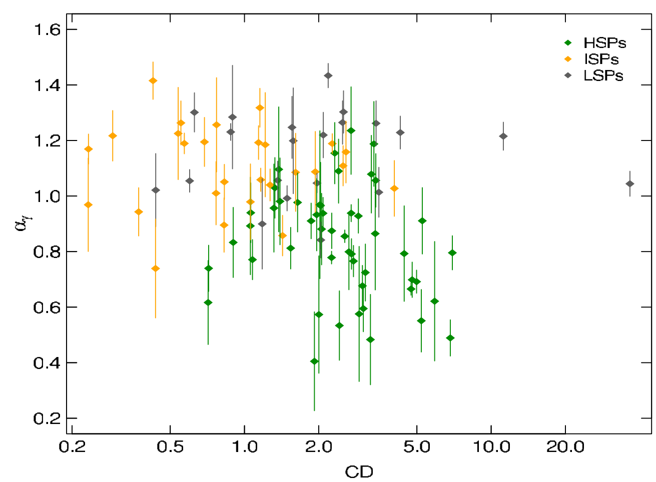


**Figure 11.** Scatterplot of the CD–$\alpha_\gamma$ distribution for BL Lacs. The three BL Lac subclasses of HSPs (green points), LSPs (black points), and ISPs (yellow points) are shown (see Section 6 for more details).

(A color version of this figure is available in the online journal.)

model. *WISE* allows to directly observe the peak or a spectral interval very close to where the synchrotron emission peaks are expected.

In this paper, we adopt the SED classification criterion for the BL Lacs for the *Fermi–WISE* blazars sample distinguishing HSPs, ISPs, and LSPs according to the 2LAC sample (Ackermann et al. 2011). For these three families of BL Lacs we studied the relation between the two spectral indices $\alpha_\gamma$–$\alpha_{IR}$. We note that, as shown in Figure 10, there is a clear distinction between the two classes in the $\alpha_\gamma$; however, it is more evident in the $\alpha_{IR}$ distribution (a 94% level of significance has been obtained with a K-S test). A similar distinction between BL Lacs subclasses is visible in the color–magnitude plot produced using the [3.4]–[4.6] $\mu$m color and the [3.4] $\mu$m magnitude in Figure 13 in Appendix A. The three families have clearly separated color distributions, with HSPs, ISPs, and LSPs with average values of the [3.4]−[4.6] $\mu$m color 0.72, 0.94, and 1.02, respectively. Finally, we calculate the correlation coefficient between the variables $\alpha_\gamma$ and $\alpha_{IR}$, finding $r_s = 0.61$ ($p$-value negligible), implying that the two variables are correlated within a high level of significance. In Figure 11, the three different BL Lacs classes in the CD versus $\alpha_\gamma$ plane are shown. In this case, the CD distributions of the HSPs and LSPs are similar (at a 70% level of confidence, obtained with a K-S test), while, for the ISPs and the HSPs, the null hypothesis can be rejected to an 87% level of significance.

## 7. SUMMARY AND DISCUSSION

We have presented the infrared characterization of a sample of blazars detected in the $\gamma$-ray. In order to perform our selection, we considered all the blazars in the ROMA-BZCAT catalog (Massaro et al. 2010) that are associated with a $\gamma$-ray source in the 2FGL (The *Fermi*-LAT Collaboration 2011). Then, we searched for infrared counterparts in the *WISE* archive adopting the same criteria described in Massaro et al. (2011a; see also Section 2 for more details). The 296 *WISE* counterparts of the ROMA-BZCAT–*Fermi* blazars constitute our sample (i.e., the *Fermi–WISE* blazars' sample). This more accurate characterization of a sample of blazars, as obtained by combining infrared and $\gamma$-ray observations, will provide crucial clues for the understanding the unassociated *Fermi* objects (Massaro et al. 2011c), since we expect most of them to be blazar candidates.

We find that the *Fermi–WISE* blazars cover a very limited region of the [3.4]−[4.6]−[12]−[22] $\mu$m color–color plane, narrower than the similar locus found for the complete blazars population of the ROMA-BZCAT seen by *WISE* (i.e., the so-called WBS; Massaro et al. 2011b; see Figure 1). In particular, we show how the separation between the *Fermi–WISE* blazars sample and the other extragalactic sources, not dominated by synchrotron emission, is evident even with different choices of infrared colors (see Figures 3 and 12). From the three independent infrared colors obtained with *WISE* magnitudes, we have derived the values of the spectral indices, finding that the IR spectrum of blazars is clearly consistent with a simple power law and does not show any evidence of deviation from that.

We investigate the properties of the relation between the spectral indices in the $\gamma$-rays and in the infrared. We found a clear trend between $\alpha_{IR}$–$\alpha_\gamma$ consistent with the expectations of the SSC or the EC scenarios. In particular, in the $\alpha_{IR}$–$\alpha_\gamma$ plot the dichotomy between the two main classes of blazars, BZBs and BZQs, is apparent. We also calculate the ratio between the infrared flux, integrated over the four *WISE* bands and the total $\gamma$-ray flux as reported in the 2FGL (The *Fermi*-LAT Collaboration 2011). This ratio can be used to estimate the CD parameter. We find that the CD distribution for the BZB population is more consistent with a synchrotron-dominated scenario; the BZQs, as expected, show values of CD typically higher than unity, in agreement with an inverse Compton framework and with the widely accepted EC emission model.

We also considered the BZB subclasses (i.e., HSPs, ISPs, LSPs) as defined in (Abdo et al. 2010) and we investigated their IR-to-$\gamma$-ray properties. We find a strong correlation between the spectral indices and the classification in BZB families; in particular, the HSP class appears to be very different from the LSPs in the $\alpha_{IR}$ distribution.

As already shown in Massaro et al. (2011a), blazars can be separated in the *WISE* IR colors from other sources not dominated by synchrotron emission; however, this distinction appears to be more evident when considering those selected on the basis of their $\gamma$-ray properties. For this reason, while we are aware that the results discussed in this paper cannot be generalized, in principle, to all $\gamma$ emitting blazars because of the inhomogeneity of the parent catalog, we deem the peculiar IR features of this large sample of confirmed blazars worth investigating and interesting per se. Moreover, since blazars constitute the most detected extragalactic sources at $\gamma$-ray energies, unidentified *Fermi* AGN candidates or *Fermi* unassociated objects (The *Fermi*-LAT Collaboration 2011) are likely to be unknown blazars. For this reason, we are investigating the possibility of employing these new infrared correlations as diagnostic tools to associate otherwise unassociated *Fermi* sources with blazars, and to better categorize this interesting class of extragalactic sources (Massaro et al. 2011c).

R. D'Abrusco gratefully acknowledges the financial support of the U.S. Virtual Astronomical Observatory, which is sponsored by the National Science Foundation and the National Aeronautics and Space Administration. F. Massaro is grateful to D. Harris for constructive discussions that improved the presentation of this paper. The work at SAO is partially supported by the NASA grants NNX10AD50G and NNX10AD68G. F. Massaro also acknowledges the Fondazione Angelo Della Riccia for the grant awarded him to support his research at SAO during 2011 and the Foundation BLANCEFLOR Boncompagni-Ludovisi, née Bildt for the grant awarded him in 2010 to support his research. M. Ajello and F. Massaro acknowledge support from the NASA grant NNH09ZDA001N. TOPCAT[8] (Taylor 2005) was used extensively in this work for the preparation and manipulation of the tabular data. Part of this work is based on archival data, software or on-line services provided by the ASI Science Data Center. This publication makes use of data products from the *Wide-field Infrared Survey Explorer*, which is a joint project of the University of California, Los Angeles, and the Jet Propulsion Laboratory/California Institute of Technology, funded by the National Aeronautics and Space Administration.

[8] http://www.star.bris.ac.uk/~mbt/topcat/

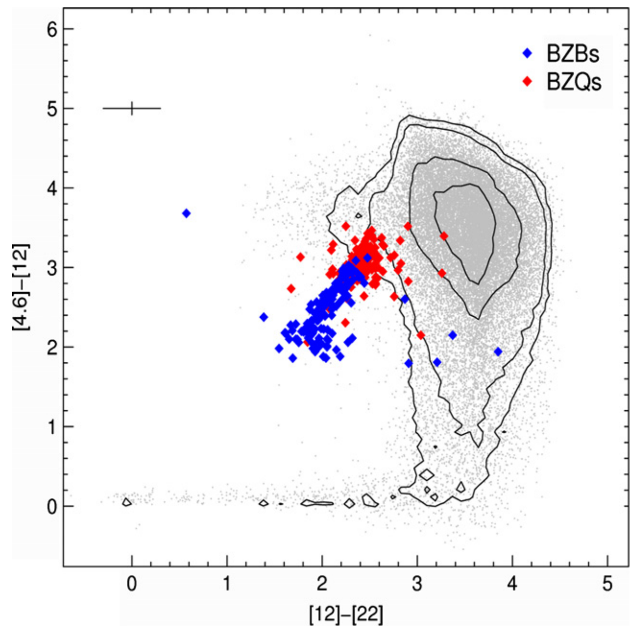


**Figure 12.** [4.6]−[12]−[22] $\mu$m color–color diagram of *Fermi*–*WISE* blazars sample sources. The two blazars classes of BZBs (blue) and BZQs (red) are shown. The background gray dots correspond to 453,420 *WISE* sources detected in a region of 56 deg$^2$ at high Galactic latitude. The isodensity curves for the *WISE* sources, corresponding to 50, 100, 500, and 2000 sources per unit area in the color–color plane, respectively, are shown (see Section 3). The black cross shown in the right bottom represents the typical error on the infrared colors.

(A color version of this figure is available in the online journal.)

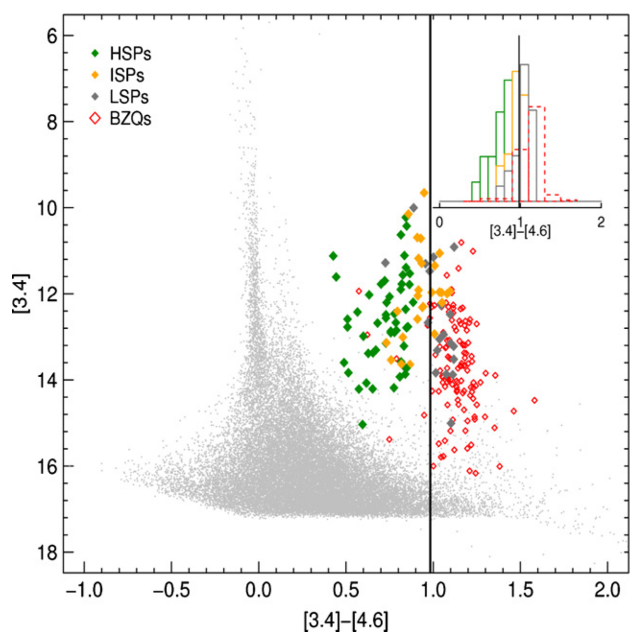


**Figure 13.** [3.4]−[4.6] vs. [3.4] color–magnitude diagram of the sources in the *Fermi*–*WISE* blazar sample. The BZQs (red symbols) and the HSPs, ISPs, and LSPs BL Lacs classes (see Section 6) are shown (green, orange, and gray symbols, respectively). The black vertical line corresponds to the color value associated with a power law with spectral index $\alpha_\nu = -1$.

(A color version of this figure is available in the online journal.)

## APPENDIX A

## ADDITIONAL PLOTS

In this Appendix, we present additional plots for the *Fermi*–*WISE* blazars sample, namely the [4.6]−[12]−[33]

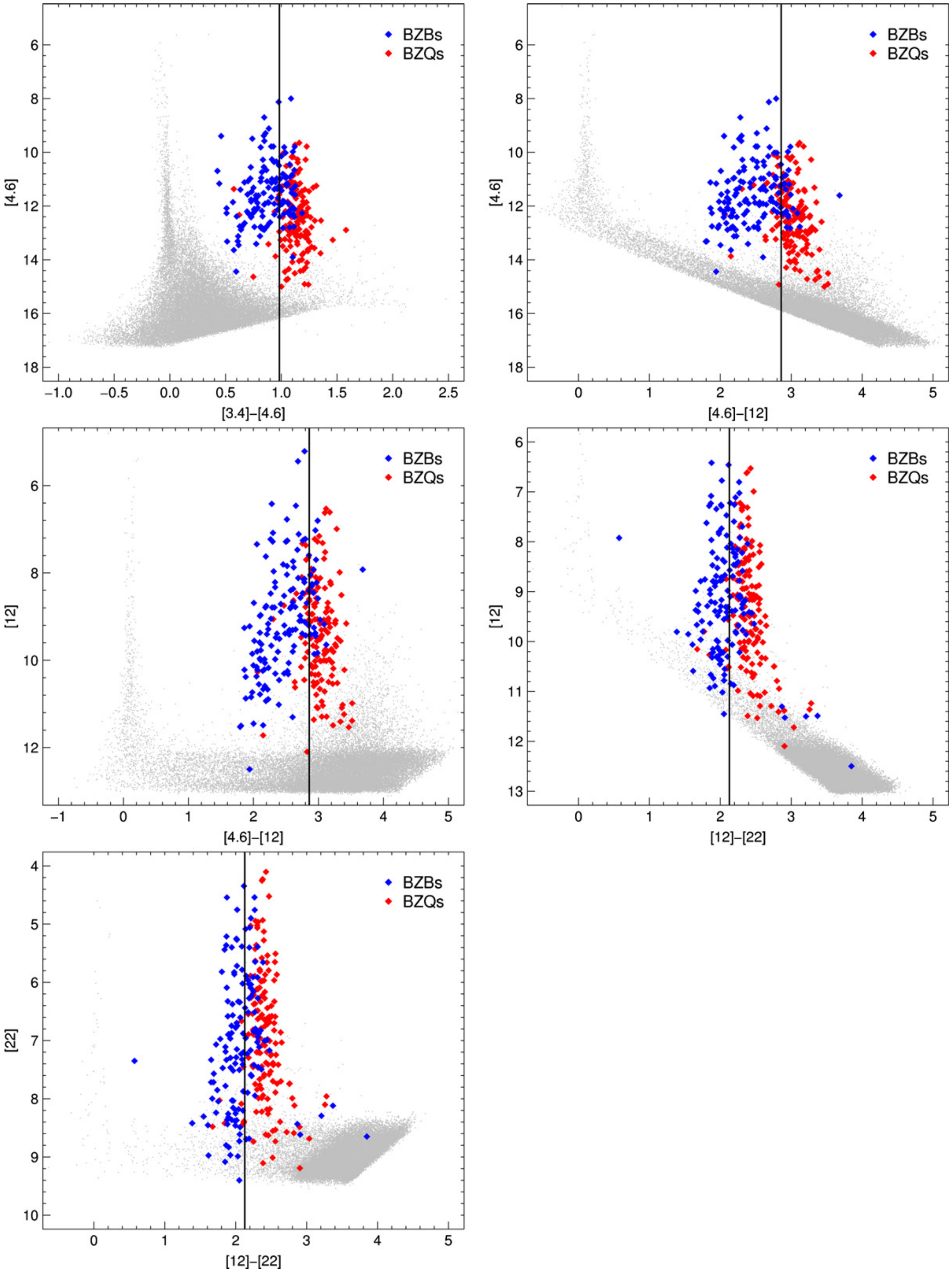


**Figure 14.** Color–magnitude diagrams of the *Fermi–WISE* sample sources. From top left: [3.4]−[4.6] vs. [4.6] plot, [4.6]−[12] vs. [4.6] plot, [4.6]−[12] vs. [12] plot, [12]−[22] vs. [12] plot, and [12]−[22] vs. [22] plot. The BZQs (red symbols) and BZBs (blue symbols) are shown in all plots. The black vertical lines correspond to the color value associated with a power law with spectral index $\alpha_\nu = -1$.

(A color version of this figure is available in the online journal.)

color–color plot (Figure 12) for BZBs and BZQs, the color–magnitude plot built using [3.4]−[4.6] color and [3.4] magnitude with the different classes of BL Lacs (Figure 13), and several color–magnitude plots with BZBs and BZQs (Figure 14) obtained using *WISE* photometric data.

## APPENDIX B

Table 1 shows the parameters of the *Fermi-WISE* blazars sample.

**Table 1**
Parameters of the *Fermi–WISE* Blazars Sample

| ROMA-BZCat Name | 2FGL Name | $m_1$ | $m_2$ | $m_3$ | $m_4$ | $\Gamma_\gamma$ | $\alpha_{IR}$ |
|---|---|---|---|---|---|---|---|
| BZBJ0035+5950 | 1ES 0033+595 | 12.26(0.03) | 11.57(0.02) | 9.56(0.05) | 7.5(0.15) | 1.87(0.07) | 0.17(0.06) |
| BZBJ0123+3420 | 1ES 0120+340 | 13.92(0.02) | 13.31(0.03) | 11.5(0.21) | 8.29() | 1.53(0.21) | −0.09(0.06) |
| BZBJ0136+3905 | B3 0133+388 | 11.9(0.02) | 11.09(0.02) | 8.99(0.03) | 7.33(0.09) | 1.69(0.04) | 0.51(0.06) |
| BZBJ0154+0823 | GB6 J0154+0823 | 11.91(0.02) | 11.0(0.02) | 8.52(0.03) | 6.57(0.07) | 1.86(0.07) | 0.81(0.06) |
| BZBJ0154+4433 | GB6 J0154+4433 | 13.25(0.03) | 12.31(0.03) | 9.98(0.05) | 8.03(0.2) | 2.01(0.26) | 0.87(0.06) |
| BZBJ0159+1047 | RX J0159.5+1047 | 12.85(0.02) | 12.06(0.02) | 9.96(0.06) | 8.24(0.3) | 2.15(0.11) | 0.44(0.06) |
| BZBJ0203+7232 | S5 0159+723 | 11.28(0.02) | 10.55(0.02) | 8.04(0.02) | 5.89(0.04) | 2.02(0.13) | 0.25(0.05) |
| BZBJ0212+2244 | MG3 J021252+2246 | 12.36(0.02) | 11.52(0.02) | 9.29(0.05) | 7.47(0.21) | 2.03(0.11) | 0.59(0.06) |
| BZBJ0217+0837 | ZS 0214+083 | 10.69(0.02) | 9.78(0.02) | 7.26(0.02) | 5.25(0.03) | 1.94(0.09) | 0.78(0.06) |
| BZBJ0222+4302 | 3C 66A | 9.55(0.02) | 8.7(0.02) | 6.42(0.02) | 4.54(0.03) | 1.85(0.02) | 0.6(0.05) |
| BZBJ0238+1636 | AO 0235+164 | 11.78(0.02) | 10.66(0.02) | 7.7(0.02) | 5.39(0.03) | 2.02(0.02) | 1.39(0.05) |
| BZBJ0243+7120 | S5 0238+711 | 12.95(0.03) | 11.89(0.02) | 9.33(0.03) | 7.03(0.09) | 1.9(0.16) | 1.23(0.07) |
| BZBJ0258+2030 | MG3 J025805+2029 | 12.84(0.03) | 11.82(0.02) | 9.48(0.05) | 7.52(0.22) | 2.19(0.17) | 1.1(0.06) |
| BZBJ0303−2407 | PKS 0301−243 | 11.11(0.02) | 10.28(0.02) | 7.96(0.02) | 6.09(0.05) | 1.94(0.03) | 0.57(0.06) |
| BZBJ0303+4716 | 4C +47.08 | 11.08(0.02) | 9.98(0.02) | 7.02(0.02) | 4.76(0.02) | 2.24(0.07) | 1.35(0.05) |
| BZBJ0304−2832 | RBS 0385 | 15.04(0.04) | 14.44(0.06) | 12.5() | 8.65() | 1.62(0.21) | −0.13(0.12) |
| BZBJ0316−2607 | RBS 0405 | 12.99(0.03) | 12.24(0.02) | 10.06(0.05) | 8.45(0.24) | 1.87(0.14) | 0.33(0.06) |
| BZBJ0316+0904 | GB6 J0316+0904 | 11.56(0.02) | 10.74(0.02) | 8.47(0.03) | 6.58(0.07) | 1.81(0.07) | 0.54(0.06) |
| BZBJ0319+1845 | RBS 0413 | 13.31(0.03) | 12.64(0.03) | 10.55(0.09) | 8.49() | 1.55(0.11) | 0.09(0.07) |
| BZBJ0321+2326 | MG3 J032201+2336 | 12.67(0.03) | 11.88(0.02) | 9.77(0.05) | 7.46(0.13) | 2.09(0.12) | 0.43(0.06) |
| BZBJ0325−1646 | RBS 0421 | 13.15(0.02) | 12.42(0.03) | 10.37(0.06) | 8.38(0.27) | 1.97(0.16) | 0.26(0.06) |
| BZBJ0326+0225 | 1H 0323+022 | 12.98(0.03) | 12.38(0.03) | 10.24(0.07) | 8.36(0.28) | 2.06(0.1) | −0.11(0.06) |
| BZBJ0334−4008 | PKS 0332−403 | 11.94(0.02) | 10.84(0.02) | 7.92(0.02) | 5.65(0.03) | 2.19(0.04) | 1.33(0.06) |
| BZBJ0334−3725 | PMN J0334−3725 | 11.47(0.02) | 10.49(0.02) | 7.87(0.02) | 5.78(0.04) | 1.99(0.05) | 0.99(0.06) |
| BZBJ0340−2119 | PKS 0338−214 | 11.99(0.02) | 11.0(0.02) | 8.22(0.02) | 6.03(0.04) | 2.43(0.14) | 1.02(0.06) |
| BZBJ0357−4955 | PKS 0355−500 | 12.32(0.02) | 11.38(0.02) | 8.81(0.02) | 6.87(0.06) | 1.74(0.18) | 0.87(0.06) |
| BZBJ0424+0036 | PKS 0422+00 | 11.15(0.02) | 10.15(0.02) | 7.47(0.02) | 5.38(0.03) | 2.3(0.07) | 1.05(0.06) |
| BZBJ0428−3756 | PKS 0426−380 | 10.84(0.02) | 9.81(0.02) | 7.11(0.02) | 4.9(0.03) | 1.95(0.02) | 1.13(0.05) |
| BZBJ0430−2507 | PMN J0430−2507 | 13.69(0.03) | 12.85(0.03) | 10.32(0.06) | 8.44(0.27) | 2.2(0.19) | 0.56(0.07) |
| BZBJ0433+2905 | MG2 J043337+2905 | 15.01(0.06) | 13.9(0.06) | 11.3(0.18) | 8.43() | 2.04(0.05) | 1.35(0.13) |
| BZBJ0434−2015 | TXS 0431−203 | 13.39(0.03) | 12.41(0.03) | 9.8(0.04) | 7.59(0.14) | 2.22(0.13) | 1.01(0.06) |
| BZBJ0448−1632 | RBS 0589 | 13.93(0.03) | 13.12(0.03) | 10.89(0.08) | 8.97(0.33) | 1.91(0.12) | 0.49(0.07) |
| BZBJ0449−4350 | PKS 0447−439 | 10.43(0.02) | 9.58(0.02) | 7.28(0.02) | 5.44(0.03) | 1.86(0.02) | 0.61(0.05) |
| BZBJ0507+6737 | 1ES 0502+675 | 12.56(0.03) | 11.83(0.02) | 9.85(0.04) | 8.3(0.23) | 1.49(0.07) | 0.26(0.06) |
| BZBJ0509+0541 | TXS 0506+056 | 10.71(0.02) | 9.78(0.02) | 7.28(0.02) | 5.27(0.03) | 2.06(0.04) | 0.84(0.05) |
| BZBJ0536−3343 | 1RXS J053629.4−334302 | 12.98(0.02) | 12.28(0.02) | 10.22(0.05) | 7.95(0.15) | 2.39(0.06) | 0.19(0.06) |
| BZBJ0538−4405 | PKS 0537−441 | 9.09(0.02) | 8.0(0.02) | 5.21(0.02) | 3.04(0.02) | 2.01(0.02) | 1.3(0.05) |
| BZBJ0558−7459 | PKS 0600−749 | 12.25(0.02) | 11.28(0.02) | 8.67(0.02) | 6.6(0.05) | 2.09(0.14) | 0.98(0.06) |
| BZBJ0607+4739 | TXS 0603+476 | 11.18(0.02) | 10.26(0.02) | 7.8(0.02) | 5.83(0.04) | 2.05(0.06) | 0.81(0.06) |
| BZBJ0612+4122 | B3 0609+413 | 11.82(0.03) | 10.81(0.02) | 8.12(0.02) | 6.02(0.04) | 2.03(0.05) | 1.09(0.06) |
| BZBJ0617+5701 | 87GB 061258.1+570222 | 11.97(0.03) | 10.98(0.02) | 8.36(0.02) | 6.33(0.05) | 1.9(0.1) | 1.02(0.06) |
| BZBJ0625+4440 | GB6 J0625+4440 | 12.92(0.03) | 11.94(0.02) | 9.3(0.03) | 7.29(0.1) | 1.91(0.14) | 1.0(0.06) |
| BZBJ0629−1959 | PKS 0627−199 | 12.38(0.03) | 11.26(0.02) | 8.41(0.02) | 6.16(0.04) | 2.19(0.06) | 1.42(0.06) |
| BZBJ0650+2503 | 1ES 0647+250 | 12.2(0.03) | 11.47(0.02) | 9.37(0.04) | 7.72(0.17) | 1.59(0.08) | 0.27(0.06) |
| BZBJ0710+5908 | 1H 0658+595 | 12.59(0.02) | 12.08(0.02) | 10.22(0.06) | 8.18(0.19) | 1.53(0.12) | −0.38(0.06) |
| BZBJ0712+5033 | GB6 J0712+5033 | 12.27(0.02) | 11.22(0.02) | 8.46(0.02) | 6.27(0.06) | 2.06(0.07) | 1.19(0.06) |
| BZBJ0721+7120 | S5 0716+71 | 9.1(0.02) | 8.13(0.02) | 5.44(0.02) | 3.4(0.02) | 2.01(0.02) | 0.98(0.05) |
| BZBJ0730+3307 | 1RXS J073026.0+330727 | 12.79(0.03) | 11.94(0.02) | 9.67(0.05) | 8.0(0.2) | 1.89(0.18) | 0.6(0.06) |
| BZBJ0738+1742 | PKS 0735+17 | 11.3(0.02) | 10.34(0.02) | 7.74(0.02) | 5.72(0.04) | 2.05(0.03) | 0.92(0.05) |
| BZBJ0744+7433 | MS 0737.9+7441 | 13.37(0.03) | 12.72(0.03) | 10.74(0.09) | 8.83() | 1.8(0.14) | 0.05(0.07) |
| BZBJ0753+5352 | 4C +54.15 | 13.87(0.03) | 12.79(0.03) | 9.86(0.05) | 7.49(0.13) | 2.01(0.09) | 1.27(0.07) |
| BZBJ0754+4823 | GB1 0751+485 | 11.97(0.03) | 10.92(0.02) | 8.15(0.02) | 5.91(0.04) | 2.19(0.09) | 1.19(0.06) |
| BZBJ0757+0956 | PKS 0754+100 | 12.0(0.02) | 10.92(0.02) | 8.04(0.02) | 5.66(0.04) | 2.19(0.06) | 1.28(0.06) |
| BZBJ0805+7534 | RX J0805.4+7534 | 12.42(0.02) | 11.86(0.02) | 9.8(0.04) | 8.04(0.16) | 1.68(0.07) | −0.21(0.06) |
| BZBJ0809+5218 | 1ES 0806+524 | 11.78(0.02) | 11.07(0.02) | 8.96(0.03) | 7.11(0.11) | 1.94(0.06) | 0.18(0.05) |
| BZBJ0811+0146 | OJ 014 | 13.88(0.03) | 12.77(0.03) | 9.65(0.05) | 7.17(0.1) | 2.26(0.08) | 1.38(0.07) |
| BZBJ0814+6431 | GB6 J0814+6431 | 11.29(0.02) | 10.36(0.02) | 7.84(0.02) | 5.86(0.04) | 2.26(0.08) | 0.86(0.05) |
| BZBJ0816−1311 | PMN J0816−1311 | 12.9(0.03) | 12.12(0.02) | 10.12(0.05) | 8.15(0.21) | 1.8(0.06) | 0.4(0.06) |
| BZBJ0816+5739 | SBS 0812+578 | 12.76(0.02) | 11.91(0.02) | 9.51(0.04) | 7.41(0.1) | 1.98(0.11) | 0.63(0.06) |
| BZBJ0817+3243 | RX J0817.9+3243 | 14.18(0.03) | 13.41(0.04) | 11.02(0.12) | 8.99(0.44) | 2.19(0.15) | 0.39(0.08) |
| BZBJ0818+4222 | S4 0814+42 | 12.7(0.03) | 11.58(0.02) | 8.59(0.03) | 6.27(0.05) | 2.14(0.03) | 1.41(0.06) |
| BZBJ0817−0933 | TXS 0815−094 | 12.43(0.03) | 11.42(0.02) | 8.78(0.03) | 6.51(0.06) | 2.04(0.09) | 1.06(0.06) |
| BZBJ0819+2747 | 5C 07.119 | 13.3(0.03) | 12.24(0.02) | 9.43(0.04) | 6.99(0.08) | 2.26(0.22) | 1.23(0.06) |
| BZBJ0819−0756 | RX J0819.2−0756 | 14.21(0.03) | 13.64(0.04) | 11.49(0.16) | 8.12(0.26) | 1.58(0.24) | −0.19(0.08) |
| BZBJ0834+4403 | B3 0831+442 | 12.85(0.03) | 11.91(0.02) | 9.31(0.04) | 7.2(0.09) | 2.04(0.19) | 0.87(0.06) |
| BZBJ0839+1802 | TXS 0836+182 | 12.76(0.03) | 11.88(0.02) | 9.39(0.04) | 7.39(0.12) | 2.46(0.2) | 0.72(0.06) |

**Table 1**
(Continued)

| ROMA-BZCat Name | 2FGL Name | $m_1$ | $m_2$ | $m_3$ | $m_4$ | $\Gamma_\gamma$ | $\alpha_{IR}$ |
|---|---|---|---|---|---|---|---|
| BZBJ0839+3540 | FIRST J083943.3+354001 | 13.54(0.03) | 12.64(0.03) | 10.31(0.08) | 8.36(0.33) | 1.92(0.18) | 0.73(0.07) |
| BZBJ0844+5312 | BZB J0844+5312 | 13.64(0.03) | 12.77(0.03) | 10.25(0.06) | 8.25(0.3) | 2.09(0.15) | 0.66(0.06) |
| BZBJ0847+1133 | RX J0847.1+1133 | 13.38(0.03) | 12.76(0.03) | 10.87(0.12) | 8.68(0.42) | 1.48(0.16) | −0.03(0.07) |
| BZBJ0856+2057 | PMN J0856−1105 | 13.5(0.03) | 12.6(0.03) | 10.06(0.08) | 7.9() | 2.14(0.14) | 0.76(0.07) |
| BZBJ0902+2050 | NVSS J090226+205045 | 12.05(0.03) | 11.13(0.02) | 8.71(0.03) | 6.7(0.07) | 2.01(0.11) | 0.79(0.06) |
| BZBJ0910+3329 | Ton 1015 | 12.2(0.02) | 11.31(0.02) | 8.89(0.03) | 6.97(0.08) | 1.94(0.11) | 0.71(0.06) |
| BZBJ0915+2933 | B2 0912+29 | 12.07(0.02) | 11.32(0.02) | 9.05(0.03) | 7.19(0.1) | 1.87(0.06) | 0.32(0.06) |
| BZBJ0929+5013 | GB6 J0929+5013 | 12.93(0.03) | 11.93(0.02) | 9.13(0.03) | 6.85(0.06) | 1.98(0.14) | 1.07(0.06) |
| BZBJ0929+8612 | S5 0916+864 | 12.86(0.02) | 11.84(0.02) | 9.09(0.03) | 6.84(0.06) | 2.05(0.09) | 1.13(0.06) |
| BZBJ0940+6148 | RX J0940.3+6148 | 13.83(0.03) | 13.32(0.03) | 11.52(0.14) | 8.62() | 2.08(0.14) | −0.36(0.07) |
| BZBJ0945+5757 | GB6 J0945+5757 | 12.52(0.02) | 11.75(0.02) | 9.39(0.03) | 7.46(0.08) | 2.16(0.14) | 0.37(0.06) |
| BZBJ0958+6533 | S4 0954+65 | 11.06(0.02) | 10.02(0.02) | 7.22(0.02) | 5.08(0.03) | 2.42(0.07) | 1.16(0.06) |
| BZBJ1018+5911 | TXS 1015+594 | 13.54(0.03) | 12.78(0.03) | 10.3(0.06) | 8.2(0.21) | 2.18(0.19) | 0.35(0.07) |
| BZBJ1019+6320 | GB6 J1019+6319 | 12.82(0.02) | 11.81(0.02) | 9.1(0.03) | 6.96(0.06) | 2.18(0.19) | 1.09(0.06) |
| BZBJ1058−8003 | PKS 1057−79 | 11.52(0.02) | 10.45(0.02) | 7.6(0.02) | 5.4(0.03) | 2.05(0.09) | 1.27(0.05) |
| BZBJ1110+7133 | 87GB 110723.4+715023 | 13.73(0.03) | 12.89(0.03) | 10.67(0.07) | 8.61(0.26) | 2.1(0.22) | 0.6(0.07) |
| BZBJ1136+7009 | Mkn 180 | 11.12(0.02) | 10.69(0.02) | 8.69(0.02) | 6.75(0.06) | 1.74(0.08) | −0.62(0.05) |
| BZBJ1223+8040 | S5 1221+80 | 13.52(0.03) | 12.4(0.02) | 9.44(0.03) | 7.11(0.07) | 2.26(0.08) | 1.4(0.06) |
| BZBJ1312−2156 | PKS 1309−216 | 12.06(0.03) | 11.12(0.02) | 8.79(0.03) | 6.9(0.1) | 2.02(0.07) | 0.9(0.06) |
| BZBJ1352−4412 | PKS 1349−439 | 12.6(0.03) | 11.51(0.02) | 8.69(0.03) | 6.52(0.07) | 2.13(0.17) | 1.32(0.06) |
| BZBJ1357+0128 | RX J1357.6+0128 | 13.68(0.03) | 12.85(0.03) | 10.45(0.08) | 8.46(0.37) | 2.28(0.16) | 0.56(0.07) |
| BZBJ1359−3746 | PMN J1359−3746 | 12.74(0.03) | 11.86(0.02) | 9.31(0.03) | 7.23(0.1) | 1.63(0.17) | 0.7(0.06) |
| BZBJ1418−0233 | BZB J1418−0233 | 11.95(0.02) | 11.08(0.02) | 8.79(0.03) | 7.07(0.1) | 1.7(0.07) | 0.68(0.06) |
| BZBJ1427+2348 | PKS 1424+240 | 10.22(0.02) | 9.38(0.02) | 7.08(0.02) | 5.21(0.03) | 1.78(0.02) | 0.59(0.05) |
| BZBJ1439−1531 | PKS 1437−153 | 13.41(0.03) | 12.33(0.03) | 9.38(0.04) | 7.17(0.12) | 2.4(0.16) | 1.28(0.07) |
| BZBJ1440+0610 | PMN J1440+0610 | 13.01(0.03) | 12.18(0.03) | 9.81(0.05) | 8.42(0.3) | 2.16(0.11) | 0.54(0.06) |
| BZBJ1442+1200 | 1ES 1440+122 | 12.77(0.02) | 12.26(0.02) | 10.38(0.07) | 8.37() | 1.41(0.18) | −0.38(0.06) |
| BZBJ1443−3908 | PKS 1440−389 | 11.7(0.02) | 10.97(0.02) | 8.79(0.03) | 6.89(0.08) | 1.77(0.06) | 0.24(0.06) |
| BZBJ1501+2238 | MS 1458.8+2249 | 11.39(0.02) | 10.55(0.02) | 8.21(0.02) | 6.33(0.05) | 1.77(0.07) | 0.6(0.05) |
| BZBJ1503−1541 | RBS 1457 | 13.74(0.03) | 13.12(0.03) | 10.93(0.13) | 9.08(0.54) | 1.8(0.15) | −0.08(0.07) |
| BZBJ1506+0814 | PMN J1506+0814 | 12.9(0.03) | 12.15(0.02) | 9.98(0.05) | 7.87(0.16) | 1.96(0.16) | 0.34(0.06) |
| BZBJ1516+1932 | PKS 1514+197 | 12.26(0.02) | 11.2(0.02) | 8.3(0.02) | 6.09(0.05) | 2.46(0.16) | 1.23(0.06) |
| BZBJ1517−2422 | AP Librae | 10.0(0.02) | 9.11(0.02) | 6.46(0.02) | 4.34(0.02) | 2.05(0.04) | 0.72(0.06) |
| BZBJ1522−2730 | PKS 1519−273 | 13.84(0.12) | 12.82(0.08) | 9.83(0.1) | 7.61(0.36) | 2.22(0.05) | 1.09(0.24) |
| BZBJ1534+3715 | RGB J1534+372 | 13.45(0.03) | 12.81(0.03) | 10.84(0.09) | 8.7(0.37) | 2.15(0.16) | 0.0(0.07) |
| BZBJ1540+8155 | 1ES 1544+820 | 12.9(0.02) | 12.2(0.02) | 10.15(0.04) | 8.26(0.17) | 1.48(0.16) | 0.16(0.06) |
| BZBJ1546+0819 | 1RXS J154604.6+081912 | 13.58(0.03) | 12.76(0.03) | 10.59(0.08) | 8.97(0.42) | 1.57(0.21) | 0.51(0.07) |
| BZBJ1548−2251 | PMN J1548−2251 | 12.49(0.02) | 11.76(0.02) | 9.64(0.04) | 7.78(0.15) | 1.93(0.13) | 0.26(0.04) |
| BZBJ1552+0850 | TXS 1549+089 | 12.28(0.03) | 11.29(0.02) | 8.57(0.03) | 6.44(0.06) | 2.0(0.16) | 1.02(0.06) |
| BZBJ1555+1111 | PG 1553+113 | 10.63(0.02) | 9.82(0.02) | 7.62(0.02) | 5.82(0.04) | 1.67(0.02) | 0.51(0.06) |
| BZBJ1607+1551 | 4C +15.54 | 13.31(0.02) | 12.29(0.02) | 9.41(0.04) | 7.0(0.08) | 2.23(0.06) | 1.12(0.06) |
| BZBJ1610−6649 | PMN J1610−6649 | 12.46(0.03) | 11.69(0.02) | 9.59(0.04) | 7.85(0.15) | 1.7(0.06) | 0.4(0.06) |
| BZBJ1630+5221 | TXS 1629+524 | 13.63(0.03) | 12.81(0.02) | 10.66(0.06) | 8.8(0.26) | 2.03(0.1) | 0.52(0.06) |
| BZBJ1642−0621 | TXS 1639−062 | 13.45(0.03) | 12.26(0.02) | 9.18(0.03) | 6.82(0.08) | 2.37(0.13) | 1.59(0.06) |
| BZBJ1653+3945 | Mkn 501 | 9.86(0.02) | 9.4(0.02) | 7.34(0.02) | 5.4(0.03) | 1.74(0.03) | −0.52(0.05) |
| BZBJ1719+1745 | PKS 1717+177 | 12.48(0.03) | 11.38(0.02) | 8.46(0.02) | 6.24(0.04) | 1.84(0.06) | 1.33(0.06) |
| BZBJ1725+1152 | 1H 1720+117 | 11.77(0.02) | 10.95(0.02) | 8.76(0.03) | 6.97(0.08) | 1.93(0.06) | 0.53(0.06) |
| BZBJ1725+5851 | 7C 1724+5854 | 12.59(0.02) | 11.68(0.02) | 9.2(0.03) | 7.33(0.08) | 2.26(0.17) | 0.79(0.06) |
| BZBJ1728+5013 | I Zw 187 | 12.02(0.02) | 11.39(0.02) | 9.17(0.02) | 7.15(0.07) | 1.83(0.13) | −0.02(0.05) |
| BZBJ1730+3714 | GB6 J1730+3714 | 13.14(0.02) | 12.41(0.02) | 10.17(0.04) | 8.18(0.18) | 2.09(0.14) | 0.27(0.06) |
| BZBJ1739+4737 | S4 1738+47 | 13.26(0.02) | 12.18(0.02) | 9.25(0.03) | 6.94(0.06) | 2.09(0.15) | 1.26(0.06) |
| BZBJ1742+5945 | RGB 1742+597 | 12.3(0.02) | 11.36(0.02) | 8.78(0.02) | 6.78(0.05) | 2.23(0.17) | 0.88(0.05) |
| BZBJ1743+1935 | S3 1741+19 | 11.61(0.02) | 11.16(0.02) | 9.22(0.03) | 7.3(0.1) | 1.62(0.15) | −0.57(0.05) |
| BZBJ1748+7005 | S4 1749+70 | 11.96(0.02) | 10.92(0.02) | 8.14(0.02) | 5.96(0.03) | 2.04(0.06) | 1.16(0.05) |
| BZBJ1749+4321 | B3 1747+433 | 13.22(0.03) | 12.1(0.02) | 9.07(0.03) | 6.8(0.06) | 2.22(0.08) | 1.39(0.06) |
| BZBJ1756+5522 | 1RXS J175615.5+552217 | 14.07(0.03) | 13.45(0.03) | 11.45(0.09) | 9.4(0.48) | 1.79(0.17) | −0.06(0.07) |
| BZBJ1800+7828 | S5 1803+784 | 10.91(0.02) | 9.79(0.02) | 6.8(0.02) | 4.54(0.02) | 2.23(0.03) | 1.4(0.05) |
| BZBJ1806+6949 | 3C 371 | 10.15(0.02) | 9.29(0.02) | 6.77(0.02) | 4.75(0.02) | 2.19(0.04) | 0.64(0.05) |
| BZBJ1809+2910 | MG2 J180948+2910 | 12.33(0.02) | 11.37(0.02) | 8.77(0.03) | 6.74(0.06) | 2.04(0.11) | 0.95(0.06) |
| BZBJ1813+3144 | B2 1811+31 | 12.4(0.02) | 11.61(0.02) | 9.4(0.04) | 7.72(0.15) | 2.11(0.07) | 0.45(0.06) |
| BZBJ1813+0615 | TXS 1811+062 | 12.98(0.03) | 11.91(0.02) | 9.12(0.03) | 6.84(0.07) | 1.97(0.13) | 1.24(0.07) |
| BZBJ1824+5651 | 4C +56.27 | 12.24(0.02) | 11.19(0.02) | 8.22(0.02) | 5.92(0.04) | 2.43(0.04) | 1.18(0.06) |
| BZBJ1829+5402 | 1RXS J182925.7+540255 | 13.21(0.02) | 12.38(0.02) | 10.21(0.04) | 8.32(0.14) | 1.88(0.13) | 0.56(0.06) |
| BZBJ1832−5659 | PMN J1832−5659 | 13.11(0.03) | 12.14(0.02) | 9.39(0.04) | 7.23(0.09) | 2.3(0.13) | 0.95(0.06) |
| BZBJ1838+4802 | GB6 J1838+4802 | 12.87(0.03) | 12.11(0.02) | 10.0(0.04) | 8.04(0.12) | 1.72(0.1) | 0.34(0.06) |
| BZBJ1849−4314 | PMN J1849−4314 | 11.93(0.03) | 10.97(0.02) | 8.4(0.02) | 6.34(0.05) | 2.02(0.09) | 0.93(0.06) |

**Table 1**
(Continued)

| ROMA-BZCat Name | 2FGL Name | $m_1$ | $m_2$ | $m_3$ | $m_4$ | $\Gamma_\gamma$ | $\alpha_{IR}$ |
|---|---|---|---|---|---|---|---|
| BZBJ1917−1921 | 1H 1914−194 | 11.53(0.03) | 10.66(0.02) | 8.33(0.02) | 6.38(0.06) | 1.91(0.06) | 0.66(0.06) |
| BZBJ1918−4111 | PMN J1918−4111 | 12.95(0.03) | 11.96(0.02) | 9.41(0.04) | 7.32(0.09) | 1.84(0.06) | 1.02(0.06) |
| BZBJ1921−1607 | PMN J1921−1607 | 12.38(0.03) | 11.6(0.02) | 7.92(0.06) | 7.35(0.24) | 1.74(0.1) | 0.39(0.06) |
| BZBJ1931+0937 | RX J1931.1+0937 | 11.79(0.04) | 11.12(0.03) | 9.26(0.04) | 7.57(0.12) | 2.36(0.07) | 0.09(0.08) |
| BZBJ1936−4719 | PMN J1936−4719 | 13.52(0.03) | 12.88(0.03) | 10.78(0.09) | 8.73(0.37) | 1.64(0.16) | −0.0(0.07) |
| BZBJ1945−3111 | PKS 1942−313 | 13.41(0.04) | 12.3(0.03) | 9.68(0.05) | 7.42(0.15) | 2.29(0.15) | 1.36(0.08) |
| BZBJ2005+7752 | S5 2007+77 | 11.06(0.02) | 10.02(0.02) | 7.26(0.02) | 5.06(0.02) | 2.22(0.09) | 1.16(0.05) |
| BZBJ2009−4849 | PKS 2005−489 | 10.23(0.02) | 9.49(0.02) | 7.23(0.02) | 5.36(0.03) | 1.78(0.05) | 0.29(0.05) |
| BZBJ2009+7229 | 4C +72.28 | 13.16(0.02) | 12.06(0.02) | 9.21(0.03) | 6.88(0.05) | 2.3(0.08) | 1.35(0.06) |
| BZBJ2015−0137 | PKS 2012−017 | 12.67(0.02) | 11.7(0.02) | 8.98(0.03) | 6.88(0.07) | 2.25(0.11) | 0.96(0.06) |
| BZBJ2022+7611 | S5 2023+760 | 12.2(0.02) | 11.15(0.02) | 8.25(0.02) | 6.04(0.03) | 2.32(0.07) | 1.2(0.06) |
| BZQJ0044−8422 | PKS 0044−84 | 13.73(0.03) | 12.65(0.03) | 9.81(0.03) | 7.44(0.09) | 2.53(0.11) | 1.28(0.06) |
| BZQJ0102+4214 | CRATES J0102+4214 | 14.58(0.04) | 13.5(0.04) | 10.45(0.07) | 8.0(0.18) | 2.61(0.09) | 1.29(0.08) |
| BZQJ0113+4948 | S4 0110+49 | 12.48(0.02) | 11.37(0.02) | 8.43(0.02) | 6.12(0.05) | 2.26(0.12) | 1.37(0.06) |
| BZQJ0128+4439 | GB6 J0128+4439 | 14.82(0.04) | 13.87(0.04) | 11.72(0.21) | 8.68() | 2.25(0.13) | 0.9(0.1) |
| BZQJ0136+4751 | OC 457 | 11.53(0.02) | 10.38(0.02) | 7.31(0.02) | 4.93(0.03) | 2.15(0.04) | 1.48(0.06) |
| BZQJ0205+3212 | B2 0202+31 | 14.47(0.04) | 12.89(0.03) | 9.64(0.05) | 7.2(0.1) | 2.66(0.14) | 2.75(0.08) |
| BZQJ0217+7349 | S5 0212+73 | 13.99(0.03) | 12.9(0.03) | 9.56(0.04) | 7.21(0.08) | 2.82(0.11) | 1.3(0.08) |
| BZQJ0217+0144 | PKS 0215+015 | 11.41(0.02) | 10.26(0.02) | 7.28(0.02) | 4.96(0.03) | 2.15(0.03) | 1.47(0.05) |
| BZQJ0230+4032 | B3 0227+403 | 13.78(0.03) | 12.58(0.03) | 9.66(0.04) | 7.43(0.12) | 2.63(0.06) | 1.62(0.07) |
| BZQJ0237+2848 | 4C +28.07 | 12.51(0.02) | 11.37(0.02) | 8.43(0.03) | 6.09(0.05) | 2.16(0.06) | 1.44(0.06) |
| BZQJ0245+2405 | B2 0242+23 | 15.48(0.05) | 14.45(0.07) | 11.09(0.14) | 8.63(0.34) | 2.54(0.08) | 1.14(0.15) |
| BZQJ0250+1712 | NVSS J025037+171209 | 12.95(0.03) | 12.33(0.03) | 10.27(0.07) | 8.42(0.33) | 1.84(0.17) | −0.05(0.06) |
| BZQJ0252−2219 | PKS 0250−225 | 14.28(0.03) | 13.04(0.03) | 9.81(0.05) | 7.38(0.12) | 2.19(0.05) | 1.76(0.07) |
| BZQJ0257−1212 | PB 09399 | 14.26(0.03) | 13.08(0.03) | 10.17(0.05) | 8.09(0.17) | 2.39(0.14) | 1.57(0.07) |
| BZQJ0303−7914 | PMN J0303−7914 | 14.28(0.03) | 13.06(0.03) | 10.02(0.04) | 7.53(0.09) | 2.2(0.13) | 1.7(0.07) |
| BZQJ0309+1029 | PKS 0306+102 | 12.26(0.02) | 11.15(0.02) | 8.12(0.02) | 5.78(0.04) | 2.26(0.08) | 1.39(0.06) |
| BZQJ0310+3814 | B3 0307+38 | 14.06(0.04) | 12.92(0.03) | 9.81(0.05) | 7.25(0.1) | 2.25(0.16) | 1.46(0.08) |
| BZQJ0312+0133 | PKS 0310+013 | 13.51(0.03) | 12.41(0.03) | 9.61(0.04) | 7.05(0.08) | 2.26(0.08) | 1.34(0.06) |
| BZQJ0315−1031 | PKS 0313−107 | 15.77(0.06) | 14.72(0.08) | 11.49(0.18) | 9.11() | 2.18(0.13) | 1.22(0.17) |
| BZQJ0325+2224 | TXS 0322+222 | 13.68(0.03) | 12.42(0.03) | 9.16(0.04) | 6.75(0.09) | 2.41(0.12) | 1.82(0.07) |
| BZQJ0336+3218 | NRAO 140 | 12.56(0.03) | 11.25(0.02) | 8.63(0.03) | 6.38(0.06) | 2.59(0.1) | 1.97(0.06) |
| BZQJ0339−0146 | PKS 0336−01 | 12.7(0.03) | 11.54(0.02) | 8.58(0.03) | 6.16(0.05) | 2.48(0.07) | 1.51(0.06) |
| BZQJ0348−2749 | PKS 0346−27 | 13.98(0.03) | 12.88(0.03) | 9.78(0.04) | 7.46(0.11) | 2.32(0.13) | 1.35(0.07) |
| BZQJ0349−2102 | PKS 0347−211 | 15.59(0.05) | 14.42(0.06) | 11.29(0.13) | 8.57(0.3) | 2.23(0.09) | 1.55(0.13) |
| BZQJ0402−3147 | PKS 0400−319 | 14.05(0.03) | 12.97(0.03) | 10.02(0.05) | 7.75(0.14) | 2.52(0.22) | 1.28(0.07) |
| BZQJ0403−3605 | PKS 0402−362 | 11.49(0.02) | 10.27(0.02) | 6.99(0.02) | 4.52(0.02) | 2.3(0.04) | 1.69(0.06) |
| BZQJ0405−1308 | PKS 0403−13 | 12.33(0.02) | 11.22(0.02) | 8.75(0.03) | 6.66(0.06) | 2.35(0.16) | 1.39(0.06) |
| BZQJ0413−5332 | PMN J0413−5332 | 15.18(0.04) | 14.08(0.04) | 11.09(0.08) | 8.53(0.23) | 2.41(0.09) | 1.34(0.09) |
| BZQJ0416−1851 | PKS 0414−189 | 14.86(0.04) | 13.56(0.04) | 10.35(0.06) | 7.99(0.17) | 2.2(0.09) | 1.92(0.09) |
| BZQJ0422−0643 | PMN J0422−0643 | 12.56(0.02) | 11.58(0.02) | 8.78(0.03) | 6.54(0.06) | 2.39(0.12) | 0.99(0.06) |
| BZQJ0423−0120 | PKS 0420−01 | 10.84(0.02) | 9.72(0.02) | 6.62(0.02) | 4.25(0.02) | 2.3(0.03) | 1.41(0.05) |
| BZQJ0426+0518 | PKS 0423+051 | 14.79(0.04) | 13.52(0.04) | 10.59(0.08) | 8.22(0.24) | 2.66(0.12) | 1.85(0.09) |
| BZQJ0438−1251 | PKS 0436−129 | 14.23(0.03) | 13.1(0.03) | 10.14(0.05) | 7.84(0.15) | 2.35(0.17) | 1.45(0.07) |
| BZQJ0442−0017 | PKS 0440−00 | 12.9(0.02) | 11.84(0.02) | 8.94(0.03) | 6.6(0.05) | 2.44(0.03) | 1.22(0.06) |
| BZQJ0448−2109 | PKS 0446−212 | 14.51(0.03) | 13.5(0.04) | 10.52(0.08) | 8.23(0.25) | 2.33(0.18) | 1.09(0.09) |
| BZQJ0453−2807 | PKS 0451−28 | 13.49(0.03) | 12.4(0.02) | 9.15(0.03) | 6.59(0.06) | 2.66(0.05) | 1.32(0.06) |
| BZQJ0455−4615 | PKS 0454−46 | 13.45(0.03) | 12.23(0.02) | 9.09(0.03) | 6.65(0.05) | 2.62(0.06) | 1.69(0.06) |
| BZQJ0456−3136 | PMN J0456−3135 | 14.37(0.03) | 13.29(0.03) | 10.34(0.05) | 7.7(0.11) | 2.42(0.14) | 1.28(0.07) |
| BZQJ0457−2324 | PKS 0454−234 | 12.27(0.02) | 11.14(0.02) | 8.15(0.02) | 5.81(0.03) | 2.03(0.02) | 1.41(0.06) |
| BZQJ0501−0159 | S3 0458−02 | 13.19(0.03) | 12.01(0.02) | 8.89(0.03) | 6.44(0.06) | 2.52(0.1) | 1.59(0.06) |
| BZQJ0502+0609 | PKS 0459+060 | 14.43(0.04) | 13.2(0.03) | 10.31(0.07) | 7.99(0.21) | 2.46(0.17) | 1.72(0.08) |
| BZQJ0505−0419 | S3 0503−04 | 14.93(0.04) | 13.81(0.04) | 10.52(0.08) | 8.41(0.28) | 2.21(0.14) | 1.38(0.1) |
| BZQJ0507−6104 | PMN J0507−6104 | 14.1(0.03) | 12.99(0.02) | 10.11(0.03) | 7.77(0.1) | 2.36(0.08) | 1.37(0.06) |
| BZQJ0509+1011 | PKS 0506+101 | 14.26(0.03) | 13.23(0.03) | 10.45(0.08) | 7.89(0.19) | 2.33(0.09) | 1.14(0.08) |
| BZQJ0510+1800 | PKS 0507+17 | 11.9(0.03) | 10.8(0.02) | 7.91(0.02) | 5.63(0.04) | 2.29(0.1) | 1.36(0.06) |
| BZQJ0515−4556 | PKS 0514−459 | 12.73(0.02) | 11.76(0.02) | 8.93(0.02) | 6.56(0.04) | 2.47(0.18) | 0.96(0.05) |
| BZQJ0526−4830 | PKS 0524−485 | 13.68(0.02) | 12.53(0.02) | 9.5(0.03) | 7.2(0.07) | 2.2(0.09) | 1.5(0.06) |
| BZQJ0530+1331 | PKS 0528+134 | 14.7(0.04) | 13.65(0.04) | 10.5(0.09) | 7.74(0.16) | 2.22(0.09) | 1.18(0.1) |
| BZQJ0529−0519 | PMN J0529−0519 | 14.3(0.03) | 13.42(0.04) | 10.19(0.06) | 7.83(0.17) | 2.3(0.39) | 0.71(0.09) |
| BZQJ0532−3848 | PMN J0532−3848 | 15.34(0.04) | 14.11(0.04) | 11.04(0.09) | 8.62(0.27) | 2.61(0.15) | 1.73(0.1) |
| BZQJ0532+0732 | OG 050 | 13.62(0.04) | 12.42(0.03) | 9.24(0.04) | 6.7(0.07) | 2.31(0.04) | 1.64(0.09) |
| BZQJ0533+4822 | TXS 0529+483 | 12.7(0.03) | 11.45(0.02) | 8.26(0.02) | 5.8(0.04) | 2.31(0.05) | 1.78(0.06) |
| BZQJ0539−2839 | PKS 0537−286 | 15.79(0.06) | 14.75(0.06) | 11.41(0.13) | 8.59(0.28) | 2.83(0.1) | 1.18(0.14) |
| BZQJ0607−0834 | PKS 0605−08 | 11.94(0.02) | 11.36(0.02) | 9.06(0.03) | 6.81(0.06) | 2.36(0.08) | −0.19(0.06) |
| BZQJ0610−6058 | PKS 0609−609 | 16.17(0.05) | 14.92(0.05) | 12.1(0.14) | 9.19(0.3) | 2.36(0.16) | 1.76(0.11) |

**Table 1**
(Continued)

| ROMA-BZCat Name | 2FGL Name | $m_1$ | $m_2$ | $m_3$ | $m_4$ | $\Gamma_\gamma$ | $\alpha_{IR}$ |
|---|---|---|---|---|---|---|---|
| BZQJ0635−7516 | PKS 0637−75 | 11.57(0.02) | 10.49(0.02) | 7.65(0.02) | 5.36(0.03) | 2.65(0.06) | 1.28(0.05) |
| BZQJ0701−4634 | PKS 0700−465 | 13.02(0.03) | 11.83(0.02) | 8.68(0.02) | 6.28(0.05) | 2.16(0.12) | 1.62(0.06) |
| BZQJ0713+1935 | MG2 J071354+1934 | 11.87(0.02) | 10.84(0.02) | 8.1(0.02) | 5.89(0.04) | 2.01(0.06) | 1.13(0.05) |
| BZQJ0725+1425 | 4C +14.23 | 13.42(0.03) | 12.31(0.03) | 9.43(0.04) | 6.98(0.08) | 2.04(0.04) | 1.37(0.06) |
| BZQJ0726+2153 | TXS 0723+220 | 15.11(0.08) | 13.76(0.06) | 10.54(0.09) | 8.44(0.31) | 2.59(0.14) | 2.08(0.17) |
| BZQJ0726−4728 | PMN J0726−4728 | 14.02(0.04) | 12.86(0.03) | 9.75(0.04) | 7.26(0.08) | 2.34(0.09) | 1.52(0.07) |
| BZQJ0730−1141 | PKS 0727−11 | 11.91(0.02) | 10.76(0.02) | 7.68(0.02) | 5.28(0.04) | 2.11(0.02) | 1.48(0.05) |
| BZQJ0733+5022 | TXS 0730+504 | 13.78(0.03) | 12.74(0.03) | 9.95(0.05) | 7.42(0.1) | 2.35(0.12) | 1.17(0.07) |
| BZQJ0739+0137 | PKS 0736+01 | 11.04(0.02) | 10.02(0.02) | 7.24(0.02) | 5.03(0.03) | 2.23(0.08) | 1.11(0.05) |
| BZQJ0746+2549 | B2 0743+25 | 16.11(0.08) | 14.9(0.09) | 11.39(0.17) | 8.48(0.28) | 2.85(0.11) | 1.66(0.2) |
| BZQJ0749+4510 | B3 0745+453 | 11.98(0.03) | 10.95(0.02) | 8.07(0.02) | 5.51(0.03) | 2.24(0.16) | 1.16(0.06) |
| BZQJ0750+1231 | OI 280 | 12.3(0.02) | 11.22(0.02) | 8.37(0.02) | 5.97(0.04) | 2.42(0.07) | 1.3(0.06) |
| BZQJ0805+6144 | TXS 0800+618 | 15.59(0.05) | 14.4(0.06) | 11.02(0.1) | 8.4(0.26) | 2.74(0.07) | 1.62(0.13) |
| BZQJ0808−0751 | PKS 0805−07 | 11.56(0.02) | 10.51(0.02) | 7.7(0.02) | 5.42(0.03) | 1.93(0.03) | 1.18(0.05) |
| BZQJ0824+3916 | 4C +39.23 | 14.18(0.03) | 12.95(0.03) | 9.75(0.04) | 7.24(0.09) | 2.64(0.17) | 1.73(0.07) |
| BZQJ0824+5552 | OJ 535 | 14.58(0.03) | 13.33(0.03) | 10.32(0.07) | 7.74(0.16) | 2.68(0.08) | 1.78(0.08) |
| BZQJ0830+2410 | S3 0827+24 | 13.14(0.03) | 11.94(0.02) | 8.8(0.03) | 6.49(0.06) | 2.67(0.07) | 1.64(0.06) |
| BZQJ0833+4224 | OJ 451 | 12.3(0.02) | 11.26(0.02) | 8.48(0.03) | 6.26(0.05) | 2.33(0.13) | 1.19(0.06) |
| BZQJ0839+0104 | PKS 0837+012 | 14.92(0.04) | 13.68(0.04) | 10.66(0.09) | 8.18(0.25) | 2.21(0.11) | 1.75(0.1) |
| BZQJ0841+7053 | 4C +71.07 | 13.73(0.03) | 12.59(0.03) | 9.16(0.03) | 6.68(0.06) | 2.95(0.07) | 1.47(0.06) |
| BZQJ0903+4651 | S4 0859+47 | 14.36(0.03) | 13.15(0.03) | 9.98(0.05) | 7.58(0.12) | 2.27(0.18) | 1.67(0.08) |
| BZQJ0912+4126 | B3 0908+416B | 15.18(0.04) | 14.0(0.05) | 10.94(0.09) | 8.12(0.17) | 2.3(0.17) | 1.59(0.1) |
| BZQJ0916+3854 | S4 0913+39 | 14.57(0.03) | 13.43(0.04) | 10.5(0.08) | 8.39(0.29) | 2.53(0.16) | 1.47(0.09) |
| BZQJ0920+4441 | S4 0917+44 | 13.59(0.03) | 12.36(0.03) | 9.09(0.03) | 6.58(0.07) | 2.11(0.03) | 1.73(0.07) |
| BZQJ0921+6215 | OK 630 | 14.3(0.03) | 13.14(0.03) | 10.02(0.05) | 7.42(0.1) | 2.51(0.09) | 1.55(0.07) |
| BZQJ0937+5008 | GB6 J0937+5008 | 13.19(0.03) | 12.02(0.02) | 8.91(0.03) | 6.4(0.06) | 2.5(0.15) | 1.55(0.06) |
| BZQJ0957+5522 | 4C +55.17 | 12.91(0.03) | 11.85(0.02) | 8.94(0.03) | 6.63(0.06) | 1.83(0.03) | 1.22(0.06) |
| BZQJ1044+8054 | S5 1039+81 | 12.44(0.02) | 11.33(0.02) | 8.42(0.02) | 6.12(0.04) | 2.54(0.15) | 1.39(0.06) |
| BZQJ1056+7011 | S5 1053+70 | 14.86(0.03) | 13.62(0.03) | 10.22(0.05) | 7.7(0.12) | 2.64(0.1) | 1.74(0.08) |
| BZQJ1058+8114 | S5 1053+81 | 13.37(0.03) | 12.2(0.02) | 9.04(0.03) | 6.64(0.06) | 2.58(0.09) | 1.57(0.06) |
| BZQJ1258−2219 | PKS 1256−220 | 12.85(0.03) | 11.65(0.03) | 8.72(0.03) | 6.55(0.07) | 2.3(0.07) | 1.61(0.06) |
| BZQJ1316−3338 | PKS 1313−333 | 12.77(0.03) | 11.65(0.02) | 8.68(0.03) | 6.34(0.06) | 2.31(0.06) | 1.41(0.06) |
| BZQJ1332−1256 | PMN J1332−1256 | 15.51(0.06) | 14.29(0.07) | 11.36(0.22) | 8.1(0.27) | 2.38(0.04) | 1.69(0.16) |
| BZQJ1337−1257 | PKS 1335−127 | 12.6(0.03) | 11.39(0.02) | 8.2(0.02) | 5.65(0.04) | 2.44(0.07) | 1.67(0.06) |
| BZQJ1342−2051 | PKS B1339−206 | 14.72(0.04) | 13.26(0.04) | 10.05(0.06) | 7.58(0.14) | 2.63(0.13) | 2.4(0.09) |
| BZQJ1344−1723 | PMN J1344−1723 | 13.33(0.03) | 12.19(0.03) | 9.15(0.04) | 6.9(0.09) | 1.95(0.06) | 1.47(0.06) |
| BZQJ1347−3750 | PMN J1347−3750 | 14.47(0.04) | 13.32(0.04) | 10.33(0.06) | 7.94(0.17) | 2.32(0.12) | 1.46(0.09) |
| BZQJ1351+0031 | PKS 1348+007 | 13.94(0.03) | 12.89(0.03) | 10.15(0.07) | 8.48(0.3) | 2.29(0.11) | 1.21(0.08) |
| BZQJ1354−1041 | PKS 1352−104 | 13.42(0.03) | 12.4(0.03) | 9.3(0.04) | 6.96(0.09) | 2.57(0.08) | 1.09(0.07) |
| BZQJ1357+7643 | S5 1357+76 | 14.95(0.03) | 13.76(0.03) | 10.79(0.06) | 7.99(0.13) | 2.3(0.1) | 1.63(0.07) |
| BZQJ1408−0752 | PKS B1406−076 | 13.84(0.03) | 12.54(0.03) | 9.52(0.05) | 7.2(0.13) | 2.43(0.06) | 1.93(0.07) |
| BZQJ1427−4206 | PKS B1424−418 | 11.26(0.02) | 10.17(0.02) | 7.22(0.02) | 4.94(0.03) | 1.96(0.03) | 1.32(0.05) |
| BZQJ1436+2321 | PKS B1434+235 | 14.06(0.03) | 12.79(0.03) | 9.49(0.04) | 6.86(0.07) | 2.41(0.18) | 1.84(0.07) |
| BZQJ1441−3303 | PKS 1438−328 | 14.17(0.03) | 13.04(0.04) | 10.01(0.06) | 7.62(0.15) | 2.76(0.17) | 1.44(0.08) |
| BZQJ1443+2501 | PKS 1441+25 | 15.41(0.05) | 14.34(0.06) | 11.29(0.16) | 8.73(0.4) | 2.03(0.12) | 1.25(0.13) |
| BZQJ1457−3539 | PKS 1454−354 | 13.0(0.03) | 11.92(0.02) | 9.07(0.03) | 6.89(0.07) | 2.11(0.03) | 1.28(0.06) |
| BZQJ1504+1029 | PKS 1502+106 | 13.21(0.03) | 12.05(0.02) | 9.06(0.03) | 6.62(0.06) | 2.15(0.02) | 1.54(0.06) |
| BZQJ1505+0326 | PKS 1502+036 | 13.94(0.03) | 12.95(0.03) | 9.68(0.04) | 7.03(0.09) | 2.51(0.07) | 1.0(0.07) |
| BZQJ1506+3730 | B2 1504+37 | 13.9(0.03) | 12.54(0.03) | 9.56(0.04) | 7.45(0.1) | 2.57(0.1) | 2.09(0.07) |
| BZQJ1509−4340 | PMN J1509−4340 | 14.27(0.05) | 13.14(0.04) | 10.5(0.07) | 7.74(0.14) | 2.65(0.14) | 1.44(0.11) |
| BZQJ1510−0543 | PKS 1508−05 | 13.18(0.02) | 12.01(0.02) | 9.06(0.03) | 6.59(0.07) | 2.44(0.06) | 1.55(0.06) |
| BZQJ1512−0905 | PKS 1510−08 | 11.27(0.02) | 10.17(0.02) | 7.37(0.02) | 5.06(0.03) | 2.29(0.01) | 1.32(0.06) |
| BZQJ1520+4211 | B3 1518+423 | 13.15(0.02) | 12.21(0.02) | 9.48(0.03) | 7.3(0.09) | 2.5(0.31) | 0.88(0.06) |
| BZQJ1521+4336 | B3 1520+437 | 15.62(0.05) | 14.5(0.06) | 10.98(0.1) | 8.74(0.31) | 2.99(0.16) | 1.4(0.13) |
| BZQJ1539+2744 | MG2 J153938+2744 | 14.17(0.03) | 12.95(0.03) | 9.86(0.04) | 7.41(0.1) | 1.99(0.13) | 1.68(0.07) |
| BZQJ1549+0237 | PKS 1546+027 | 12.21(0.02) | 11.13(0.02) | 8.47(0.03) | 6.22(0.05) | 2.46(0.07) | 1.27(0.06) |
| BZQJ1550+0527 | 4C +05.64 | 13.38(0.03) | 12.2(0.02) | 9.1(0.03) | 6.61(0.07) | 2.32(0.11) | 1.6(0.06) |
| BZQJ1608+1029 | 4C +10.45 | 12.56(0.03) | 11.46(0.02) | 8.6(0.03) | 6.23(0.04) | 2.33(0.1) | 1.34(0.06) |
| BZQJ1610−3958 | PMN J1610−3958 | 11.98(0.03) | 10.87(0.02) | 7.95(0.02) | 5.58(0.03) | 2.61(0.1) | 1.36(0.07) |
| BZQJ1613+3412 | OS 319 | 14.02(0.03) | 12.89(0.03) | 9.91(0.04) | 7.38(0.1) | 2.31(0.17) | 1.44(0.07) |
| BZQJ1617−7717 | PKS 1610−77 | 13.23(0.03) | 12.16(0.03) | 9.07(0.03) | 6.62(0.06) | 2.5(0.05) | 1.27(0.06) |
| BZQJ1635+3808 | 4C +38.41 | 13.09(0.03) | 11.86(0.02) | 8.51(0.02) | 5.96(0.04) | 2.25(0.03) | 1.71(0.06) |
| BZQJ1637+4717 | 4C +47.44 | 12.63(0.02) | 11.45(0.02) | 8.35(0.02) | 5.98(0.04) | 2.41(0.06) | 1.59(0.06) |
| BZQJ1640+3946 | NRAO 512 | 15.0(0.04) | 13.81(0.04) | 10.72(0.07) | 8.26(0.19) | 2.36(0.06) | 1.6(0.08) |
| BZQJ1642+3948 | 3C 345 | 11.8(0.03) | 10.63(0.02) | 7.52(0.02) | 5.13(0.03) | 2.49(0.06) | 1.54(0.06) |
| BZQJ1656+6012 | 87GB 165604.4+601702 | 14.26(0.03) | 13.26(0.03) | 10.62(0.05) | 8.18(0.14) | 2.36(0.21) | 1.03(0.06) |

**Table 1**
(Continued)

| ROMA-BZCat Name | 2FGL Name | $m_1$ | $m_2$ | $m_3$ | $m_4$ | $\Gamma_\gamma$ | $\alpha_{IR}$ |
|---|---|---|---|---|---|---|---|
| BZQJ1703−6212 | CGRaBS J1703−6212 | 12.27(0.03) | 11.26(0.02) | 8.44(0.02) | 6.19(0.04) | 2.43(0.04) | 1.07(0.06) |
| BZQJ1709+4318 | B3 1708+433 | 13.5(0.03) | 12.35(0.02) | 9.31(0.03) | 6.98(0.07) | 2.31(0.05) | 1.48(0.06) |
| BZQJ1722+1013 | TXS 1720+102 | 12.42(0.02) | 11.33(0.02) | 8.33(0.02) | 5.98(0.04) | 2.23(0.06) | 1.31(0.06) |
| BZQJ1724+4004 | S4 1722+40 | 14.16(0.03) | 13.09(0.03) | 10.0(0.04) | 7.66(0.1) | 2.34(0.06) | 1.25(0.06) |
| BZQJ1727+4530 | S4 1726+45 | 13.67(0.02) | 12.51(0.02) | 9.37(0.03) | 6.82(0.06) | 2.58(0.06) | 1.52(0.06) |
| BZQJ1728+1215 | PKS 1725+123 | 13.66(0.03) | 12.48(0.03) | 9.42(0.04) | 6.98(0.08) | 2.09(0.2) | 1.58(0.06) |
| BZQJ1728+0427 | PKS 1725+044 | 12.3(0.02) | 11.31(0.02) | 8.45(0.03) | 5.87(0.04) | 2.53(0.08) | 1.02(0.06) |
| BZQJ1730+0024 | PKS 1728+004 | 12.85(0.03) | 11.72(0.03) | 8.78(0.03) | 6.49(0.07) | 2.31(0.07) | 1.43(0.06) |
| BZQJ1733−1304 | PKS 1730−13 | 12.14(0.03) | 11.06(0.02) | 8.1(0.02) | 5.66(0.04) | 2.24(0.09) | 1.3(0.06) |
| BZQJ1734+3857 | B2 1732+38A | 13.49(0.03) | 12.31(0.02) | 9.15(0.03) | 6.79(0.06) | 2.24(0.04) | 1.58(0.06) |
| BZQJ1739+4955 | S4 1738+49 | 12.61(0.03) | 11.5(0.02) | 8.64(0.02) | 6.37(0.04) | 2.2(0.09) | 1.36(0.06) |
| BZQJ1740+5211 | 4C +51.37 | 12.33(0.02) | 11.16(0.02) | 8.16(0.02) | 5.89(0.03) | 2.5(0.04) | 1.54(0.05) |
| BZQJ1745+2252 | TXS 1742+228 | 15.21(0.04) | 14.05(0.05) | 11.08(0.1) | 8.55(0.28) | 2.87(0.17) | 1.52(0.11) |
| BZQJ1801+4404 | S4 1800+44 | 13.23(0.02) | 12.19(0.02) | 9.16(0.03) | 6.72(0.05) | 2.66(0.14) | 1.16(0.06) |
| BZQJ1818+0903 | MG1 J181841+0903 | 13.08(0.03) | 11.98(0.03) | 9.11(0.03) | 6.82(0.08) | 2.32(0.08) | 1.32(0.07) |
| BZQJ1848+3219 | B2 1846+32A | 13.36(0.03) | 12.19(0.02) | 9.13(0.03) | 6.69(0.06) | 2.38(0.09) | 1.54(0.06) |
| BZQJ1852+4855 | S4 1851+48 | 13.08(0.03) | 12.0(0.02) | 9.13(0.02) | 6.89(0.06) | 2.28(0.04) | 1.28(0.06) |
| BZQJ1903−6749 | PMN J1903−6749 | 13.46(0.03) | 12.38(0.02) | 9.49(0.03) | 7.08(0.08) | 2.49(0.1) | 1.3(0.06) |
| BZQJ1911−2006 | PKS B1908−201 | 11.27(0.02) | 10.17(0.02) | 7.16(0.03) | () | 2.21(0.05) | 1.36(0.06) |
| BZQJ1923−2104 | TXS 1920−211 | 11.09(0.02) | 10.08(0.02) | 7.33(0.02) | 5.02(0.03) | 2.1(0.04) | 1.08(0.05) |
| BZQJ1924−2914 | PKS B1921−293 | 10.81(0.02) | 9.65(0.02) | 6.53(0.02) | 4.1(0.02) | 2.43(0.05) | 1.52(0.06) |
| BZQJ1954−1123 | TXS 1951−115 | 13.68(0.04) | 12.5(0.03) | 9.45(0.05) | 7.08(0.12) | 2.25(0.05) | 1.57(0.08) |
| BZQJ1957−3845 | PKS 1954−388 | 12.35(0.02) | 11.19(0.02) | 8.28(0.02) | 5.87(0.04) | 2.36(0.05) | 1.51(0.05) |
| BZQJ1959−4246 | PMN J1959−4246 | 13.62(0.03) | 12.45(0.03) | 9.48(0.04) | 7.01(0.08) | 2.41(0.05) | 1.53(0.07) |
| BZQJ2007−4434 | PKS 2004−447 | 13.37(0.03) | 12.28(0.03) | 9.42(0.04) | 7.01(0.09) | 2.47(0.12) | 1.3(0.06) |
| BZQJ2023−1139 | PMN J2023−1140 | 15.38(0.05) | 14.63(0.08) | 11.24(0.17) | 7.96(0.21) | 2.07(0.11) | 0.32(0.16) |
| BZQJ2025−0735 | PKS 2023−07 | 13.32(0.03) | 12.08(0.02) | 8.87(0.03) | 6.33(0.06) | 2.15(0.03) | 1.75(0.06) |
| BZQJ2030−0622 | TXS 2027−065 | 14.15(0.03) | 12.93(0.03) | 9.8(0.06) | 8.03(0.26) | 2.73(0.1) | 1.7(0.08) |
| BZQJ2056−4714 | PKS 2052−47 | 12.6(0.03) | 11.31(0.02) | 7.99(0.02) | 5.54(0.04) | 2.23(0.04) | 1.89(0.06) |
| BZQJ2135−5006 | PMN J2135−5006 | 16.0(0.08) | 15.0(0.11) | 11.53(0.21) | 9.01() | 2.58(0.1) | 1.05(0.23) |
| BZQJ2147−7536 | PKS 2142−75 | 11.01(0.02) | 9.78(0.02) | 6.61(0.02) | 4.23(0.02) | 2.52(0.04) | 1.72(0.05) |
| BZQJ2202−8338 | PKS 2155−83 | 13.82(0.03) | 12.67(0.02) | 9.7(0.04) | 7.46(0.1) | 2.2(0.08) | 1.48(0.06) |

**Notes.** Column 1 contains the name of the blazer in the ROMA-BZCat catalog; Column 2: the name of the associated source from the 2FGL catalog; Columns 3–6: the values of the magnitude in the four *WISE* filters ([3.4], [4.6], [12], and [22] $\mu$m, respectively); Column 7: the $\Gamma\gamma$ photon index of the sources from the 2FGL catalog; and Column 8: the IR spectral index $\alpha_{12}$ evaluated from *WISE* magnitudes ([3.4] and [4.6]). Errors are reported in parentheses.

## REFERENCES


Abdo, A. A., Ackermann, M., Agudo, I., et al. 2010, ApJ, 716, 30
Ackermann, M., Ajello, M., Allafort, A., et al. 2011, ApJ, 743, 171
Blandford, R. D., & Rees, M. J. 1978, in BL Lac Objects (Pittsburgh, PA: Univ. Pittsburgh Press), 328
Cavaliere, A., & D'Elia, V. 2002, ApJ, 571, 226
Chen, P. S., Fu, H. W., & Gao, Y. F. 2005, New Astron., 11, 27
Cutri, R. M., Wright, E. L., Conrow, T., et al. 2011, Explanatory Supplement to the WISE Preliminary Data Release Products, 1, http://wise2.ipac.caltech.edu/docs/release/prelim/expsup/wise_prelrel_toc.html
Dermer, C. D., & Schlickeiser, R. 2002, ApJ, 575, 667
Giommi, P., Padovani, P., Polenta, G., et al. 2011, arXiv:1110.4706
Giommi, P., Piranomonte, S., Perri, M., & Padovani, P. 2005, A&A, 434, 385
Giroletti, M., Reimer, A., Fuhrmann, L., & Pavlidou, V. 2010, Accretion and Ejection in AGN: A Global View, 427, 283
Inoue, S., & Takahara, F. 1996, ApJ, 463, 555
Kovalev, Y. Y., Aller, H. D., Aller, M. F., et al. 2009, ApJ, 696, L17
León-Tavares, J., Valtaoja, E., Chavushyan, V. H., et al. 2011, MNRAS, 411, 1127
Marscher, A. P., & Gear, W. K. 1985, ApJ, 298, 114
Maselli, A., Cusumano, G., Massaro, E., et al. 2011, A&A, 531, A153
Massaro, E., Giommi, P., Leto, C., et al. 2009, A&A, 495, 691
Massaro, E., Giommi, P., Leto, C., et al. 2010, arXiv:1006.0922
Massaro, F., D'Abrusco, R., Ajello, M., Grindlay, J. E., & Smith, H. A. 2011a, ApJ, 740, L48
Massaro, F., Paggi, A., Elvis, M., & Cavaliere, A. 2011b, ApJ, 739, 73
Massaro, F., et al. 2011c, ApJ, submitted
Padovani, P., & Giommi, P. 1995, MNRAS, 277, 1477
Padovani, P., Perlman, E. S., Landt, H., Giommi, P., & Perri, M. 2003, ApJ, 588, 128
Taylor, M. B. 2005, in ASP Conf. Ser. 347, Astronomical Data Analysis Software and Systems XIV, ed. P. Shopbell, M. Britton, & R. Ebert (San Francisco, CA: ASP), 29
The *Fermi*-LAT Collaboration 2011, ApJ, submitted (arXiv:1108.1435)
Wright, E. L., Eisenhardt, P. R. M., Mainzer, A. K., et al. 2010, AJ, 140, 1868